

|   |                   |                               |                                  |   |  |
|---|-------------------|-------------------------------|----------------------------------|---|--|
| REPORT DOCUMENTATION PAGE   |                   |                               |                                  | Form Approved OMB NO. 0704-0188                       |  |
| <p>The public reporting burden for this collection of information is estimated to average 1 hour per response, including the time for reviewing instructions, searching existing data sources, gathering and maintaining the data needed, and completing and reviewing the collection of information. Send comments regarding this burden estimate or any other aspect of this collection of information, including suggestions for reducing this burden, to Washington Headquarters Services, Directorate for Information Operations and Reports, 1215 Jefferson Davis Highway, Suite 1204, Arlington VA, 22202-4302. Respondents should be aware that notwithstanding any other provision of law, no person shall be subject to any penalty for failing to comply with a collection of information if it does not display a currently valid OMB control number.</p> <p>PLEASE DO NOT RETURN YOUR FORM TO THE ABOVE ADDRESS.</p> |                   |                               |                                  |   |  |
| 1. REPORT DATE (DD-MM-YYYY)   |                   | 2. REPORT TYPE<br>New Reprint |                                  | 3. DATES COVERED (From - To)<br>-                     |  |
| 4. TITLE AND SUBTITLE<br>Gas Metal Arc Welding Process Modeling and Prediction of Weld Microstructure in MIL A46100 Armor-Grade Martensitic Steel   |                   |                               |                                  | 5a. CONTRACT NUMBER<br>W911NF-11-1-0207               |  |
|   |                   |                               |                                  | 5b. GRANT NUMBER                                      |  |
|   |                   |                               |                                  | 5c. PROGRAM ELEMENT NUMBER<br>622105                  |  |
| 6. AUTHORS<br>M. Grujicic, A. Arakere, S. Ramaswami, J. S. Snipes, R. Yavari, C-F. Yen, B. A. Cheeseman, J. S. Montgomery   |                   |                               |                                  | 5d. PROJECT NUMBER                                    |  |
|   |                   |                               |                                  | 5e. TASK NUMBER                                       |  |
|   |                   |                               |                                  | 5f. WORK UNIT NUMBER                                  |  |
| 7. PERFORMING ORGANIZATION NAMES AND ADDRESSES<br>Clemson University<br>Office of Sponsored Programs<br>300 Brackett Hall, Box 345702<br>Clemson, SC 29634 -5702  |                   |                               |                                  | 8. PERFORMING ORGANIZATION REPORT NUMBER              |  |
| 9. SPONSORING/MONITORING AGENCY NAME(S) AND ADDRESS(ES)<br>U.S. Army Research Office<br>P.O. Box 12211<br>Research Triangle Park, NC 27709-2211   |                   |                               |                                  | 10. SPONSOR/MONITOR'S ACRONYM(S)<br>ARO               |  |
|   |                   |                               |                                  | 11. SPONSOR/MONITOR'S REPORT NUMBER(S)<br>57228-EG.13 |  |
| 12. DISTRIBUTION AVAILABILITY STATEMENT<br>Approved for public release; distribution is unlimited.  |                   |                               |                                  |   |  |
| 13. SUPPLEMENTARY NOTES<br>The views, opinions and/or findings contained in this report are those of the author(s) and should not be construed as an official Department of the Army position, policy or decision, unless so designated by other documentation.   |                   |                               |                                  |   |  |
| 14. ABSTRACT<br>A conventional gas metal arc welding (GMAW) butt-joining process has been modeled using a two-way fully coupled, transient, thermal-mechanical finite-element procedure. To achieve two-way thermal-mechanical coupling, the work of plastic deformation resulting from potentially high thermal stresses is allowed to be dissipated in the form of heat, and the mechanical material model of the workpiece and the weld is made temperature dependent. Heat losses from the deposited filler-metal are accounted for by  |                   |                               |                                  |   |  |
| 15. SUBJECT TERMS<br>gas metal arc welding (GMAW), microstructure evolution, MIL A46100, process modeling   |                   |                               |                                  |   |  |
| 16. SECURITY CLASSIFICATION OF:   |                   |                               | 17. LIMITATION OF ABSTRACT<br>UU | 15. NUMBER OF PAGES                                   | 19a. NAME OF RESPONSIBLE PERSON<br>Mica Grujicic |
| a. REPORT<br>UU   | b. ABSTRACT<br>UU | c. THIS PAGE<br>UU            |                                  |   | 19b. TELEPHONE NUMBER<br>864-656-5639            |

## **Report Title**

Gas Metal Arc Welding Process Modeling and Prediction of Weld Microstructure in MIL A46100 Armor-Grade Martensitic Steel

### **ABSTRACT**

A conventional gas metal arc welding (GMAW) butt-joining process has been modeled using a two-way fully coupled, transient, thermal-mechanical finite-element procedure. To achieve two-way thermal-mechanical coupling, the work of plastic deformation resulting from potentially high thermal stresses is allowed to be dissipated in the form of heat, and the mechanical material model of the workpiece and the weld is made temperature dependent. Heat losses from the deposited filler-metal are accounted for by considering conduction to the adjoining workpieces as well as natural convection and radiation to the surroundings. The newly constructed GMAW process model is then applied, in conjunction with the basic material physical-metallurgy, to a prototypical high-hardness armor martensitic steel (MIL A46100). The main outcome of this procedure is the prediction of the spatial distribution of various crystalline phases within the weld and the heat-affected zone regions, as a function of the GMAW process parameters. The newly developed GMAW process model is validated by comparing its predictions with available open-literature experimental and computational data.

---

**REPORT DOCUMENTATION PAGE (SF298)**  
**(Continuation Sheet)**

---

Continuation for Block 13

ARO Report Number    57228.13-EG  
Gas Metal Arc Welding Process Modeling and P    ...

Block 13: Supplementary Note

© 2013 . Published in Journal of Materials Engineering and Performance, Vol. Ed. 0 22, (6) (2013), (, (6). DoD Components reserve a royalty-free, nonexclusive and irrevocable right to reproduce, publish, or otherwise use the work for Federal purposes, and to authroize others to do so (DODGARS §32.36). The views, opinions and/or findings contained in this report are those of the author(s) and should not be construed as an official Department of the Army position, policy or decision, unless so designated by other documentation.

Approved for public release; distribution is unlimited.

# Gas Metal Arc Welding Process Modeling and Prediction of Weld Microstructure in MIL A46100 Armor-Grade Martensitic Steel

*M. Grujicic, A. Arakere, S. Ramaswami, J.S. Snipes, R. Yavari, C-F. Yen, B.A. Cheeseman, and J.S. Montgomery*

*(Submitted October 16, 2012; published online December 1, 2012)*

A conventional gas metal arc welding (GMAW) butt-joining process has been modeled using a two-way fully coupled, transient, thermal-mechanical finite-element procedure. To achieve two-way thermal-mechanical coupling, the work of plastic deformation resulting from potentially high thermal stresses is allowed to be dissipated in the form of heat, and the mechanical material model of the workpiece and the weld is made temperature dependent. Heat losses from the deposited filler-metal are accounted for by considering conduction to the adjoining workpieces as well as natural convection and radiation to the surroundings. The newly constructed GMAW process model is then applied, in conjunction with the basic material physical-metallurgy, to a prototypical high-hardness armor martensitic steel (MIL A46100). The main outcome of this procedure is the prediction of the spatial distribution of various crystalline phases within the weld and the heat-affected zone regions, as a function of the GMAW process parameters. The newly developed GMAW process model is validated by comparing its predictions with available open-literature experimental and computational data.

**Keywords** gas metal arc welding (GMAW), microstructure evolution, MIL A46100, process modeling

with the prediction of the welding-induced changes in the material microstructure and properties. These aspects are reviewed briefly in the remainder of this section.

## 1. Introduction

In this study, a new fully coupled finite-element-based, process model has been developed for conventional gas metal arc welding (GMAW). The model is subsequently combined with basic physical-metallurgy concepts and principles of a prototypical high-hardness armor-grade martensitic steel MIL A46100 [Ref 1] to predict functional relationships between the basic process parameters and the spatial distribution of the material microstructure and properties within the weld region (also known as the fusion zone, FZ) and the region adjacent to the weld (the heat-affected zone, HAZ). It is argued that availability of such a process model can be beneficial relative to the attainment of the optimal GMAW process conditions and the resulting weld microstructure and properties. Based on the foregoing, the main aspects of this study are: (a) the fundamentals of the GMAW process, (b) expected, and typically observed welding-induced changes in the material microstructure and properties, and (c) a survey of the previous computational efforts dealing with the GMAW process modeling and

### 1.1 The Fundamentals of GMAW

GMAW is one of the conventional fusion-welding processes in which: (a) an electrical arc established between a continuously fed filler-metal wire-shape consumable electrode and the workpiece components to be joined is used to generate the heat required for the filler-metal melting and (b) the welding process zone is protected from the oxidizing/contaminating environment using an externally supplied shielding gas (or mixture of gases) [Ref 2]. Figure 1 shows a labeled schematic of the conventional gas metal arc butt welding process. Feeding of the filler-metal wire is usually automated during this process, to maintain a stable electrical arc. Control of other aspects of the GMAW process is typically not automated, but the operator is only required to provide/control input regarding welding-gun positioning, guidance, and travel speed.

Briefly stated, the GMAW process has these key advantages: (a) most of the commercially available metallic materials, in particular steels (including stainless steels), super alloys, aluminum alloys, etc., can be joined using this process; (b) joints in all common orientations, e.g., horizontal, inclined, vertical, and overhead, can be fabricated; (c) welds produced are clean due to the use of the (externally supplied) shielding gas; (d) comparatively high welding speeds can be achieved, especially in the case of large-gage sections; (e) the process is highly robust due to the short and stable character of the arc; (f) very high (93-98%) utilization efficiency of the filler-metal wire; and (g) GMAW is highly amenable to process automation. However, this process also has some significant shortcomings: (a) it is unsuitable for joining highly reactive/

**M. Grujicic, A. Arakere, S. Ramaswami, J.S. Snipes, and R. Yavari**, Department of Mechanical Engineering, Clemson University, Mica Grujicic, 241 Engineering Innovation Building, Clemson, SC 29634; and **C-F. Yen, B.A. Cheeseman, and J.S. Montgomery**, Army Research Laboratory—Survivability Materials Branch, Aberdeen, Proving Ground, MD 21005-5069. Contact e-mail: gmica@clemson.edu.

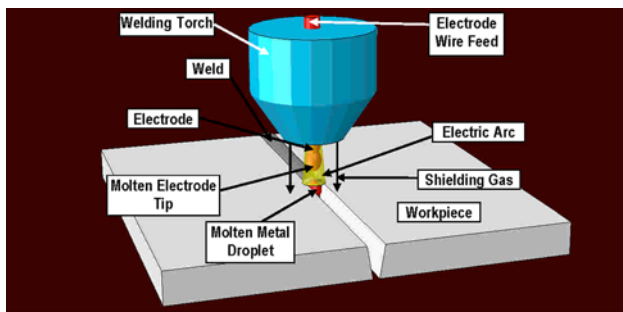


**Fig. 1** A schematic representation of the conventional GMAW process

oxidation-prone metallic materials; (b) if the process parameters are not selected appropriately, major (generally undesirable) changes in the material microstructure and properties may result in the HAZ; (c) due to its coarse microstructure and the potential porosity, the FZ may possess inferior material properties relative to those found in the heat-affected workpiece material; and (d) the bulky nature of the GMAW gun renders production of small and complex welds difficult or even infeasible.

As mentioned above, the GMAW process involves transfer of the molten filler-metal into the gap/groove between adjoining components. Depending on the selection of the GMAW process parameters, metal transfer occurs in one of the following five modes, e.g., [Ref 2]: (a) *short-circuit mode* In this case, transfer occurs during repeated (50-250 times per second) short periods (within which the electrode is in direct contact with the weld pool and, thus, the arc is absent). To achieve this mode of transfer, the feed rate must exceed the electrode melt rate. Due to the relatively low overall heat input, a shallow, fast-freezing weld puddle is produced via this mode of metal transfer. Hence, (i) this transfer mode is generally unsuitable for joining large-gage workpieces, (ii) welding may be conducted in any orientation, (iii) it can be used for sheet-metal welding, and (iv) the tendency for weldment distortions and burn-throughs is greatly reduced; (b) *globular mode* Here, metal transfer is accomplished via large (typical size is 2-4 times the electrode diameter) drops. Typically, the use of carbon dioxide as a shielding gas facilitates the development of this mode of metal transfer; (c) *spray mode* In this case, metal transfer occurs through an axially directed spray consisting of small droplets of the filler-metal melt. The mode is promoted by the use of high currents which give rise to the formation of high number density melt droplets; (d) *pulsed mode* This mode is promoted by the use of high (several hundred times per second) frequency, alternating welding voltage. The voltage cycles about a mean value that is sufficiently high to produce a steady arc, with metal transfer accomplished only at peak levels of the welding voltage. In this transfer mode, the GMAW process: (i) allows through the selection of the peak voltage and frequency, greater control of the deposition rate, (ii) results in a reduction in the overall lower heat input to the weldment, and (iii) is suitable for the fabrication of welds of all common orientations; and (e) *high current density mode* Here, selective combinations of high wire/electrode feed rate, electrode length (a longer length causes higher temperature and, in turn, filler-wire tip melting), and shielding gas (a proper selection of the shielding gas can increase molten-metal surface tension, promoting droplet formation at the molten electrode-tip) are used to obtain

a particular state of the arc which enables significantly higher molten-metal transfer rates. Two regimes of this metal transfer mode are generally identified: (i) the non-rotational regime, which is observed at lower welding currents and in the presence of helium-/carbon dioxide-rich shielding gases. This regime is characterized by a narrower/stationary axial arc and a localized, deeper FZ and (ii) the rotational regime, which is observed at higher welding currents and is characterized by a wider, helically moving rotational arc and a wider and shallower FZ.

The key parameters of the GMAW process are as follows [Ref 2]: (a) temporal profile and mean value of the welding current/voltage, (b) composition of the filler-metal, (c) electrode length and diameter, (d) filler-wire feed rate, (e) electrode travel speed, (f) composition and flow-rate of the shielding gas, (g) workpiece material(s), and (h) geometry, size, and orientation of the weld.

## 1.2 Steel-Weldment Microstructure Evolution During the Welding Process

As stated earlier, GMAW involves the melting and transfer of a filler metal into a gap/groove separating the components to be joined. In addition to producing the heat required for the filler-metal melting, the electric arc is also responsible for electro-magnetic stirring of the molten metal within the resulting weld pool. This process significantly affects heat transfer within the weld pool and, in turn, temperature distribution and thermal history of the material in the entire weld region [Ref 3]. As the welding torch (Fig. 1) travels along the weld line, the previously formed weld pool begins to cool and ultimately solidifies. Upon complete solidification of the material within the weld pool, solid material within the solidified FZ may undergo several (material-system and thermal history dependent) solid-state phase transformations and microstructure evolution/reorganization processes [Ref 4-6]. As the FZ solidifies and cools, the material in the HAZ first experiences heating (the extent of which is dependent on the distance from the weld center-line) and subsequent cooling, and this thermal history also gives rise to a number of solid-phase transformations and microstructure evolution/reorganization processes. Due to the aforementioned changes experienced by the filler-metal within the FZ and the base metal within the HAZ, it is generally found that the overall mechanical (e.g., strength, toughness, ductility, etc.) and environmental resistance (e.g., corrosion resistance) properties of the weldments are greatly affected by the welding-induced thermal histories of the material within the FZ and the HAZ.

In this study, microstructure evolution in a GMAW butt weld of a prototypical armor grade high-hardness martensitic steel (MIL A46100) is investigated computationally. As pointed out earlier, material within both the FZ and the HAZ may undergo a series of phase transformations following deposition of the molten filler-metal into the weld groove. Leaving out displacive/diffusionless (e.g., bainitic, martensitic) phase transformations and the diffusional phase-transformations which produce microstructural constituents (e.g., pearlite) from austenite, as well as alloy-carbide precipitation reactions, the material within the FZ generally undergoes the following sequence of phase transformations: liquid  $\rightarrow$   $\delta$ -ferrite  $\rightarrow$   $\gamma$ -austenite  $\rightarrow$   $\alpha$ -ferrite, while material within the HAZ undergoes the following sequence of phase transformations: martensite  $\rightarrow$   $\gamma$ -austenite  $\rightarrow$   $\alpha$ -ferrite [Ref 2]. Numerous experimental investigations [Ref 1] have established that: (a)

the solidification process within the weld pool is responsible for the overall quality/soundness of the weld; and (b) the material region within the FZ or HAZ which is associated with the most inferior (thermal-history-governed and material-system dependent) mechanical properties governs the overall performance of the weldment [Ref 7, 8]. These observations/findings have been rationalized as the effect of the material thermal history on the rate and the extent of various solid-state phase transformations and microstructure evolution/reorganization processes.

As stated earlier, this study deals with the computational investigation of the material microstructure within the FZ and HAZ during GMAW of MIL A46100A (butt) welds. Historically, microstructure and properties of the GMAW joints have been investigated experimentally using various real-time and post-mortem techniques, including: (a) *dilatometric measurements* [Ref 9] Within this technique, the progress of the assumed/predicted phase transformations is related to dimensional changes to the test sample; (b) *spatially and time-resolved x-ray diffraction* [Ref 3] The use of this synchrotron-radiation-based technique enables not only monitoring of the progress but also identification of the nature of the phase transformation; and (c) *post-mortem as-welded microstructure characterization* In this case, various microscopy, diffraction, scattering, and spectroscopy-based techniques are utilized to characterize and quantify the as-welded microstructure. In general, this approach is of a destructive character and requires sectioning of the weldment and special preparation of the exposed surfaces. To infer the progress of phase transformation during GMAW from the post-mortem as-welded microstructure characterization results, typically detailed knowledge of the thermodynamics and kinetics of the attendant phase transformations is required.

### 1.3 Existing GMAW Process Models

An overview of the public-domain literature identified a number of efforts dealing with numerical modeling and simulations of the GMAW process. Closer examination of these efforts reveals that they all could be classified into three categories of GMAW modeling/simulation approaches: (a) this class of GMAW models focuses on heat transfer from the arc to the stationary weld pool [Ref 10–12], while mass transfer from the electrode to the weld pool via the process of molten metal droplets generation and transfer is neglected; (b) within this class of GMAW models, both heat and mass transfer aspects of the process are analyzed [Ref 13, 14] while accounting for a number of GMAW-specific phenomena such as (i) electrode-tip melting, (ii) droplet formation/detachment/transfer and impingement onto the weld pool, (iii) dynamics of the weld pool and the interactions between the arc/plasma, and (iv) molten-metal transfer and the weld pool surface; and (c) GMAW models which fall into this category focus on the weld pool heat/mass transfer and solidification processes and subsequent solid-state microstructure phase transformations and microstructure-evolution processes [Ref 3, 15, 16]. Typically, these GMAW models: (i) assume that the weld pool exists from the onset of simulation and that its initial temperature and velocity fields are known and (ii) combine the heat/mass transfer analyses with the basic physical-metallurgy principles to predict the evolution of microstructure during the welding process. It should be pointed out that the GMAW model developed in this study falls into this category of the GMAW models.

## 1.4 Main Objective

The main objective of this article is to extend the GMAW process model which was developed in our recent work to predict the distribution of the material microstructure in different FZ/HAZ locations of a prototypical low-carbon steel (AISI 1005) under a given set of welding/process parameters. The main extension of the model will include addressing the specifics of phase transformations and microstructural evolution/reorganization processes which are unique to the subject material MIL A46100 armor-grade high-hardness martensitic steel.

As mentioned earlier, the rate and extent of various phase transformations within different weld regions is governed by the associated thermal histories. These histories are predicted, as a function of the process parameters, weld geometries, and filler/base-metal thermal properties, by the GMAW process model [Ref 16]. The results obtained from the extended GMAW process model will be compared with available public-domain experimental data to provide model validation/verification.

## 1.5 Organization of the Article

A brief overview of the basic physical-metallurgy concepts and principles related to MIL A46100A and the associated family of armor-grade high-hardness martensitic steels is provided in section 2. A brief overview of the GMAW process model developed in our recent work [Ref 16] and details regarding its extension are provided in section 3. The key results pertaining to the effect of GMAW process parameters on the spatial distribution of the principal crystallographic phases and microconstituents within the FZ and HAZ of a MIL A46100 butt weld are presented and discussed in section 4. The main conclusions resulting from this study are summarized in section 5.

## 2. Basic Physical Metallurgy of MIL A46100

### 2.1 Identification

MIL A46100 is a rolled homogenous armor (RHA) plain steel whose chemical composition, material processing, and plate-fabrication routes as well as the resulting material-microstructure and properties are governed by the specification MIL STD A46100 [Ref 17]. This steel falls into the category of air-quenchable, self-tempered, high-hardness, low-alloy martensitic steels. It is generally available in plate thicknesses up to 2 in. (50.8 mm) and is primarily intended for use in light-armor applications. As mentioned above, plates of this material are produced by hot rolling steel castings and during this process material microstructure is homogenized while most of the microstructural imperfections/defects are removed. The as-fabricated RHA should be distinguished from the face-hardened metallic armor, in which various hardening techniques are employed to increase strength/hardness of the armor strike-face.

### 2.2 Chemical Composition

MIL A46100 has the following nominal chemical composition expressed in weight percents: C—0.28, Mn—0.90, Si—0.53, Cr—0.30, Mo—0.24, Ni—0.19, Ti—0.03, Cu—0.18, Al—0.02, V—0.007, S—0.002.



### 2.3 Typical Properties

In the as-received (i.e., hot-rolled) condition, MIL A46100 typically possesses the following general, mechanical, thermal, and thermo-mechanical properties: density,  $\rho = 7850 \text{ kg/m}^3$ ; Brinell hardness,  $H_B = 480\text{--}540$ ; yield strength,  $\sigma_y = 1000\text{--}1100 \text{ MPa}$ ; ultimate tensile strength,  $UTS = 1750\text{--}1800 \text{ MPa}$ ; uniform elongation,  $\epsilon_{UTS} = 10\text{--}13\%$ ; Charpy V-notch absorbed energy,  $U_{\text{Charpy-V}} = 25\text{--}30 \text{ J}$ ; specific heat,  $C_V = 440\text{--}520 \text{ J/kg}\cdot\text{K}$ ; thermal conductivity,  $k = 35\text{--}50 \text{ W/m}\cdot\text{K}$ ; and coefficient of linear thermal expansion,  $\alpha = 11\text{--}12 \times 10^{-6} \text{ K}^{-1}$ .

### 2.4 Weldability

MIL A46100 steel plates can be readily joined using conventional welding techniques. Details regarding the pre-welding treatment, welding procedure, and post-welding handling are governed by the MIL-DTL-46100E specification. In the case of GMAW, MIL A46100 steel plates do not need to be heated prior to welding, while the joining surfaces must be clean and dry, and the necessary precautions taken against hydrogen pick-up. Other (typical) GMAW conditions as defined by the aforementioned specification include: (a) “no gap” groove geometrical parameters: land = 1.5 mm, included angle =  $60^\circ$ ; (b) number of weld passes = 1; (c) filler wire diameter = 1.6 mm; (d) filler metal transfer mode—spray; (e) type of shielding gas—98% Ar/2%  $\text{O}_2$ ; (f) shielding gas flow rate =  $1.2 \text{ m}^3/\text{h}$ ; (g) gas nozzle inner diameter = 12.7 mm; (h) contact-tip-to-workpiece distance = 17.5 mm; (i) welding voltage = 27.5 V; (j) welding current = 310–315 A; (k) wire feed speed = 400–450 cm/min; (l) weld gun travel speed = 30–35 cm/min; and (m) predicted heat input = 1626 kJ/m.

### 2.5 Distinct Zones of the GMAW Weld Region

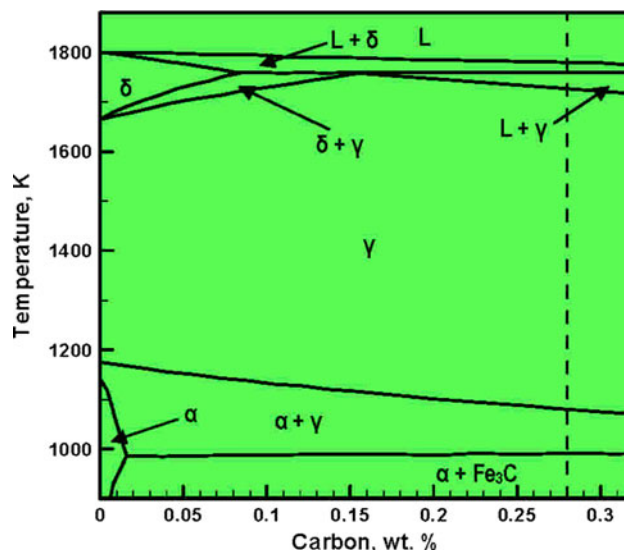
A GMAW weld region typically consists of two main zones: (a) the FZ containing mainly the solidified filler-metal and (b) the HAZ containing the work-piece base metal which has undergone microstructural (and, to a lesser extent, chemical composition) changes during welding. The HAZ, in turn, can be divided into several sub-zones which are listed (and described) below in the ascending order of distance from the weld centerline: (i) the coarse-grained sub-zone, which contains mainly martensite formed during cooling from austenite with a large grain size due to its exposure to high temperatures (within the single-phase austenite region); (ii) the fine-grained sub-zone, which contains martensite and bainite formed during cooling from austenite with a relatively smaller grain size due to its exposure to lower temperatures (within the single-phase austenite region); (iii) the so-called inter-critical sub-zone, which has been exposed to the temperatures sufficiently high to form austenite but not high enough to fully austenitize the material. Consequently, this sub-zone contains both non-austenite phases (i.e., ferrite and alloy-carbides) present at the highest temperature to which this sub-zone was exposed and the products of austenite decomposition during cooling (i.e., martensite, bainite, ferrite); and (iv) the so-called sub-critical zone, within which the material was never exposed to a temperature sufficiently high to result in the formation of austenite. Consequently, the microstructure in this sub-zone consists mainly of tempered martensite (i.e., a mixture of ferrite and carbides).

### 2.6 Phase Diagram

Following the standard practice, the equilibrium state of MIL A46100 (as defined by the crystalline phases present, their

chemical compositions and their volume fractions) at different temperatures (and under atmospheric pressure) can be determined using the corresponding multi-component (equilibrium) phase diagram. In this diagram, the axes are the concentrations of all the MIL A46100 main alloying elements (i.e., C, Mn, Si, Cr, Mo, etc.) and temperature. However, the construction of such a multi-component phase diagram is highly impractical due to its multi-dimensional nature. Instead, the corresponding “quasi-binary” para-equilibrium Fe-C phase diagram is typically used. Within this two-dimensional, alloy-system-dependent diagram, it is assumed that the concentration of each non-carbon alloying element is the same as that in the overall material itself. In other words, it is assumed that due to the low diffusivity of the non-carbon alloying elements relative to that of carbon, their partitioning between various phases does not take place. The quasi-binary para-equilibrium phase diagram of MIL A46100 is displayed in Fig. 2. Examination of Fig. 2 reveals that the MIL A46100 quasi-binary phase diagram is quite similar to the true-binary Fe-C phase diagram, except that the values of the characteristic temperatures and concentrations have been slightly modified. This finding is consistent with the fact that MIL A46100 is a low-alloy steel in which the chemical composition (and, consequently, the Gibbs free energy function) of the key crystalline phases has not changed significantly relative to that in the Fe-C binary system. In addition, volume fractions of the additional phases not present in the Fe-C system such as  $\text{Mo}_2\text{C}$ ,  $(\text{Cr},\text{Mo})_{23}\text{C}_6$  and  $(\text{Ti},\text{V})\text{N}$  are quite small.

As partitioning of alloying elements does take place in MIL A46100, the quasi-binary phase diagram displayed in Fig. 2 has relatively limited utility. On the other hand, while, as pointed out earlier, there are challenges associated with the graphical representation of a multi-component phase diagram, one can extract and readily display specific details contained within the phase diagram. For example, for the steel in question, one can compute the equilibrium volume fraction of all the phases present at different temperatures and the atmospheric pressure. This was done in Ref. 15 using the materials-thermodynamics commercial software ThermoCalc [Ref 18] and the results of this calculation are shown in



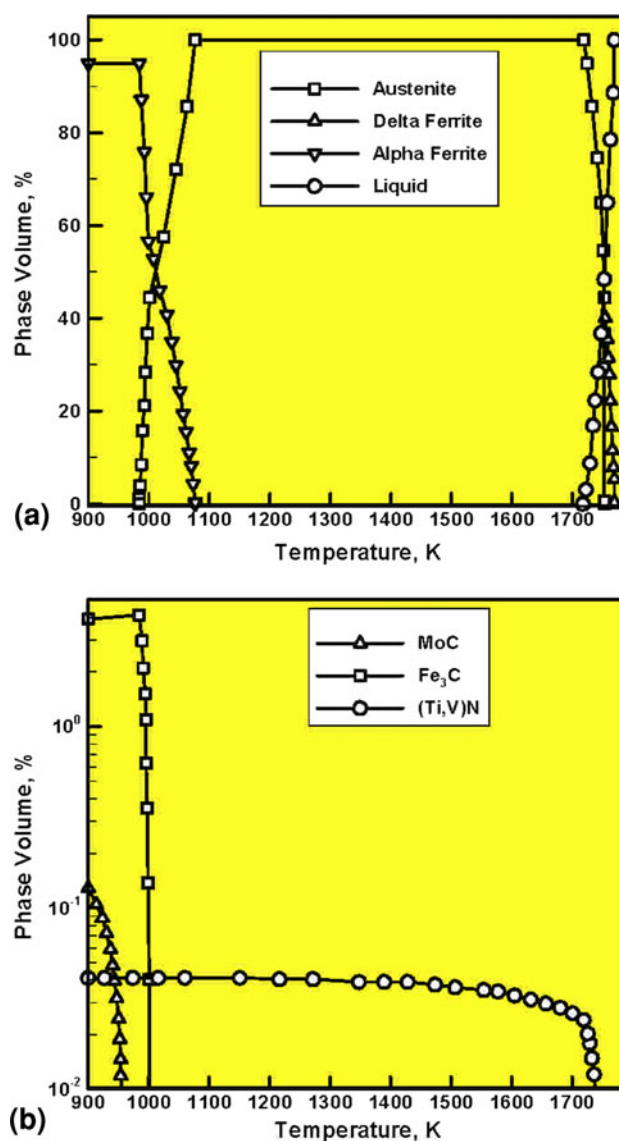
**Fig. 2** A portion of the quasi-binary para-equilibrium Fe-C phase diagram corresponding to the non-carbon alloy additions at a level nominally found in MIL A46100

Fig. 3(a) and (b). Examination of Fig. 3(a) enables the determination of the following MIL A46100 characteristic temperatures: (a) the liquidus temperature ( $=1772$  K) defined as the temperature at which the volume fraction of the liquid first begins to deviate from 100% during cooling, (b) the peritectic-transformation temperature ( $=1750$  K) defined as the temperature at which austenite first appears during cooling, (c) the solidus temperature ( $=1720$  K) defined as the lowest temperature at which the liquid is still present, (d) the  $Ac_3$  temperature ( $=1076$  K) defined as the temperature at which  $\alpha$ -ferrite first appears during cooling, and (e) the  $Ac_1$  temperature ( $=982$  K) defined as the temperature at which austenite vanishes during cooling. On the other hand, examination of Fig. 3(b) reveals that: (a) (Ti,V)(N,C) primary precipitates first appear at temperatures slightly above the solidus temperature, due to the associated high super-saturation of the residual liquid with the alloying elements and their volume fraction does not change significantly during subsequent cooling. In addition, it is seen that cementite begins to form during cooling at a temperature in the  $Ac_1$ - $Ac_3$  range while MoC forms at temperatures below  $Ac_1$ .

## 2.7 Time-Temperature-Transformation (TTT) Diagram(s)

As mentioned earlier, during cooling of the material within the FZ, austenite (a high-temperature  $\gamma$ -phase with face-centered-cubic, FCC crystal structure) undergoes transformation into a number of low-temperature ferrite (a low-temperature  $\alpha$ -phase with body-centered-cubic, BCC crystal structure)-based phases/micro-constituents. Some of these transformations are not predicted by the phase diagram as they occur under finite cooling-rate conditions while the phase diagram predicts the state of the material only under extremely slow cooling conditions. To overcome this shortcoming of the phase diagram, additional, material-specific time-based diagrams are used. The first diagram of this kind is the so-called TTT diagram. A series of TTT diagrams for MIL A46100, as a function of the maximum temperature experienced by austenite, is depicted in Fig. 4(a) to (e). In general, diagrams of this type are constructed experimentally by quenching the steel in question from a temperature greater than  $Ac_1$  to (and holding at) a desired temperature below  $Ac_1$  and determining the time of the onset of austenite decomposition, the so-called incubation time. Major advances have been made in the capabilities of the computational methods and tools used for the construction of fairly accurate TTT diagrams. For example, the TTT diagrams displayed in Fig. 4(a) to (e) were determined computationally in Ref 15 using a proprietary computer code.

The TTT diagrams displayed in Fig. 4(a) to (e) are adopted in this study. The (missing) TTT diagrams associated with the pre-quench austenite temperatures other than the ones referenced in Fig. 4(a) to (e) are obtained using a simple linear interpolation scheme. Examination of the TTT diagrams displayed in Fig. 4(a) to (e) reveals the presence of three (complete or partial) C-shaped curves. The two high-temperature curves labeled  $F_s$  and  $F_f$  represent, respectively, the loci of the incubation times for the allotriomorphic ferrite (a variation of ferrite possessing a featureless external morphology which does not reflect the symmetry of the associated underlying crystalline structure) and acicular/Widmanstätten ferrite (a version of ferrite possessing an acicular/lenticular-plate morphology which grows into the untransformed austenite from the austenite/austenite grain boundaries and/or



**Fig. 3** Equilibrium volume fractions of all the phases present in MIL A46100 as a function of temperature (and at atmospheric pressure) [Ref 15]

allotriomorphic-ferrite/austenite interfaces). The lower C-shaped curve,  $B_s$ , is associated with the displacive bainitic phase transformation which produces a lath or acicular-shaped bainitic phase in which atomic diffusion of iron and alloying elements other than carbon is suppressed. Further examination of Fig. 4(a) to (e) reveals the presence of two low-temperature horizontal lines. These lines, labeled as  $M_s$  and  $M_f$ , denote, respectively, the temperatures at which displacive/diffusionless martensitic phase transformation starts and finishes. The product of this transformation is martensite, a solid solution with a highly distorted tetragonal crystal structure (due to high levels of carbon super-saturation) and acicular morphology. Finally, it is seen that Fig. 4(a) to (e) contains two high-temperature horizontal lines. These lines, labeled as  $Ac_1$  and  $Ac_3$ , represent the highest temperature at which, during cooling, austenite volume fraction decreases below 1.0 and the highest temperature at which austenite volume fraction drops to 0.0, respectively.



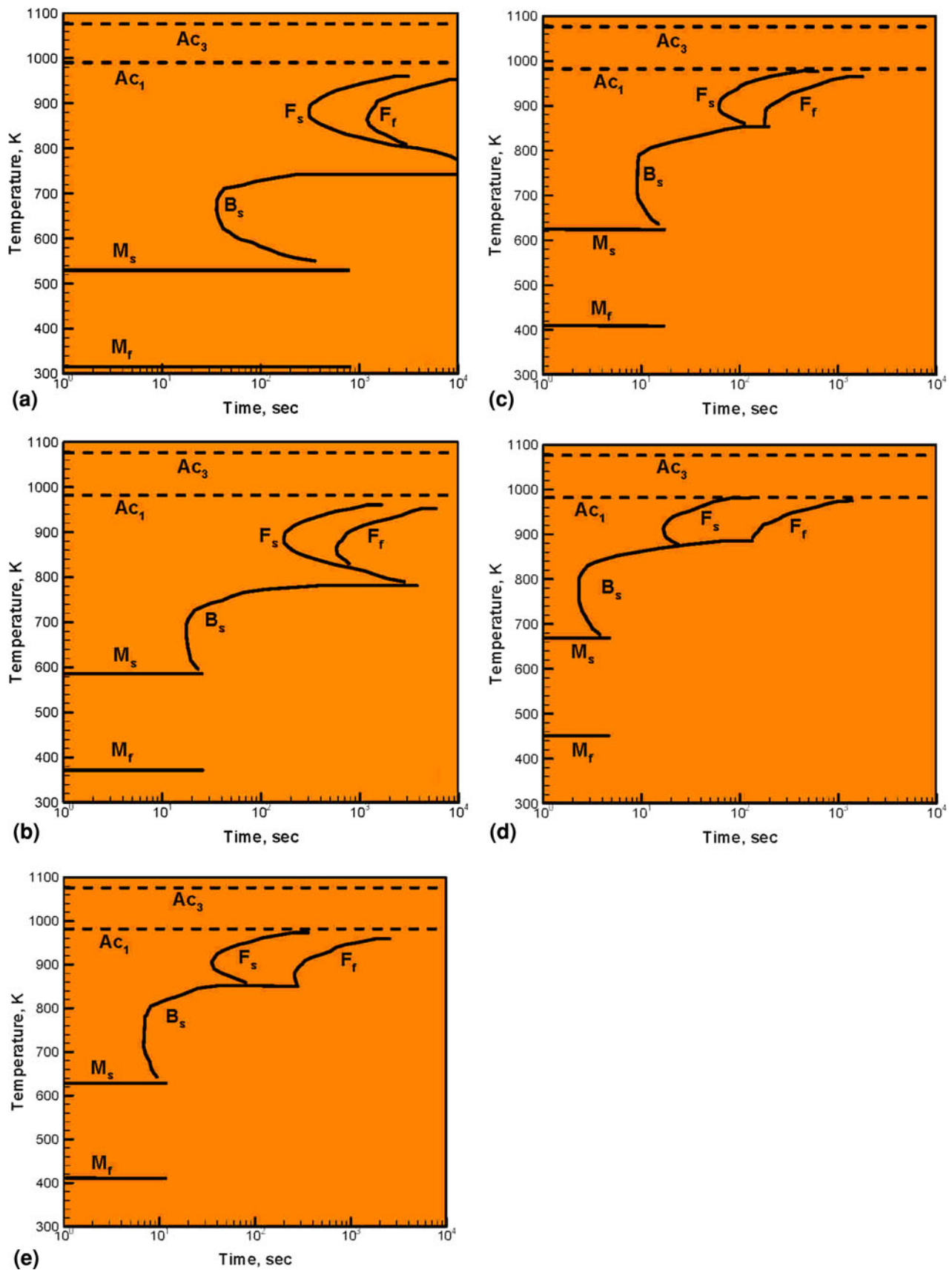


**Fig. 4** The TTT diagrams for MIL A46100 steel equilibrated initially at: (a) 993 K, (b) 1003 K, (c) 1053 K, (d) 1076 K, and (e) 1330 K. Symbols  $F_s$ ,  $F_r$ , and  $B_s$  are used to denote the locus of the temperature vs. time conditions at which austenite begins to transform, respectively, into allotrophic ferrite, acicular ferrite, and bainite, respectively. Symbols  $Ac_3$ ,  $Ac_1$ ,  $M_s$ , and  $M_r$  have their common meanings (please see text for details)

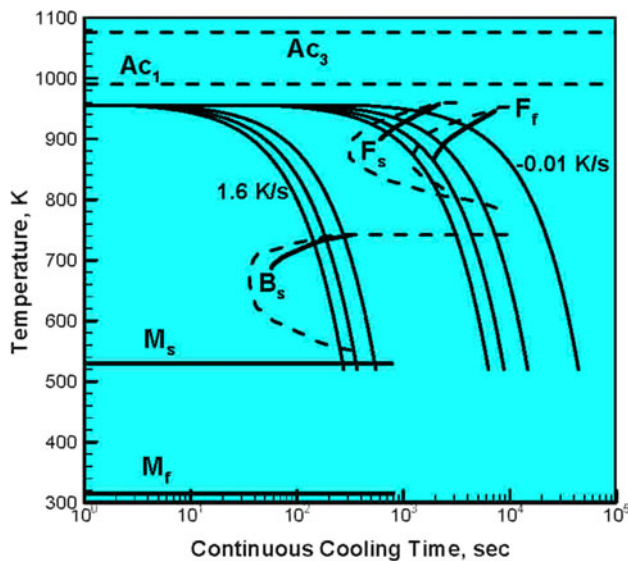


**Fig. 5** MIL A46100 CCT diagram corresponding to the TTT diagram displayed in Fig. 4(a). CCT curves and the  $M_s$  and  $M_f$  temperature lines are denoted using heavy solid lines, while representative cooling curves are shown as light solid lines. The TTT curves and the  $Ac_1$  and  $Ac_3$  temperature lines are denoted using dashed lines

## 2.8 Continuous-Cooling-Transformation (CCT) Diagram(s)

As pointed out above, a TTT diagram is obtained under particular thermal-history conditions which include quenching of austenite from a super- $Ac_1$  temperature to (and holding at) a sub- $Ac_1$  temperature until the associated austenite-decomposition phase transformation begins to take place. Within an actual GMAW process, no material point within the weld region is generally expected to be associated with this type of thermal history. Instead, one would typically expect a thermal history which is characterized by continuous cooling from the maximum temperature to which austenite has been subjected. Thus, a diagram is needed which can be used to display various types of austenite-decomposition phase transformations under arbitrary continuous-cooling conditions. The so-called Scheil additive rule is adopted in this study to model austenite-decomposition under continuous-cooling conditions. According to this rule:

$$\int_0^t \frac{dt'}{\tau(T(t'))} = 1, \quad (\text{Eq 1})$$

where  $t$  is the (non-isothermal) incubation time associated with the cooling history  $T(t')$ ,  $\tau(T)$  is the corresponding locus of the temperature-dependent incubation times,  $t'$  is a dummy-time variable and  $t' = 0$  corresponds to the moment when, during cooling, the temperature of a given material point becomes equal to the corresponding (i.e., austenite  $\rightarrow$  allotriomorphic ferrite, austenite  $\rightarrow$  Widmanstätten ferrite, or austenite  $\rightarrow$  bainite) equilibrium transformation temperature. In the case of the austenite  $\rightarrow$  allotriomorphic-ferrite transformation, this temperature corresponds to the  $Ac_3$  temperature while in the cases of the austenite  $\rightarrow$  Widmanstätten ferrite and austenite  $\rightarrow$  bainite transformations, the corresponding temperatures can be operationally defined as the horizontal asymptotes for the  $F_f$  and  $B_s$  partial C-shaped curves, Fig. 4(a) to (e). Examination of Eq 1 reveals that the Scheil

additive rule simply postulates that the material has to reach the same critical state of incubation for the particular austenite-decomposition phase-transformation to begin. The progress of the material toward this critical incubation state, at a given temperature  $T$  during cooling, is simply defined by the  $\frac{dt'}{\tau(T(t'))}$  ratio, and the time integral of this quantity at the onset of phase transformation, hence, has to be equal to 1.0.

The procedure described above is demonstrated using the TTT diagram shown earlier in Fig. 4(a) to construct the corresponding CCT diagram, Fig. 5. The diagram displayed in Fig. 5 is obtained under particular continuous-cooling conditions, i.e., the ones associated with constant cooling rates. It should be noted that both TTT and CCT curves are shown in Fig. 5 and, for improved clarity, the TTT curves are denoted in this figure using dashed lines. For the same reason, the resulting CCT curves are drawn as heavy, while representative cooling curves are denoted as light solid lines. It should be noted that, due to the athermal nature of the martensitic transformation, the  $M_s$  transformation temperature is not affected by the details of the material cooling history. Consequently, the  $M_s$  and  $M_f$  horizontal lines coincide with their TTT counterparts.

## 2.9 Phase Volume Fractions Within the FZ

As pointed out earlier, the main objective of this study is to enable predictions relative to the spatial distributions of the phase volume fractions within the FZ and HAZ. The information provided by the aforementioned phase, TTT and CCT diagrams are necessary, but not sufficient, input for a phase volume-fraction determination procedure. That is, in addition to knowing the temperature under a given thermal history at which a particular phase transformation will take place, models and data are needed to determine the rate of growth/evolution of the newly formed phases. Such models are developed in this section for the FZ material points. In the next section, the corresponding models will be presented for the HAZ material points. Two sets of models were deemed necessary, considering the fact that the material points within the FZ and the HAZ generally possess quite different thermal histories. That is, within the FZ thermal history is dominated by the continuous cooling of austenite (formed from the liquid phase during solidification), while within the HAZ thermal history involves initial heating of the as-received martensitic microstructure and subsequent cooling of the austenite phase (formed from the martensitic phase during heating).

**2.9.1 Phase Volume Fraction Calculations.** As mentioned earlier, within the FZ, depending on the cooling history, austenite may transform into one or more of the following phases: allotriomorphic ferrite, acicular ferrite, bainite, and/or martensite. In the remainder of this section, procedures are presented for computing the final volume fractions of the phases formed during austenite decomposition within different portions of the FZ.

**2.9.2 Allotriomorphic-Ferrite Volume Fraction.** As discussed in our prior work [Ref 16], austenite grains formed during solidification are, for the most part, of a columnar shape and aligned with the direction of the maximum heat extraction. For modeling purposes, the cross section of the columnar austenite grains is typically idealized as being of a regular hexagonal shape. In other words, as shown schematically in Fig. 6(a), the columnar austenite grains are assumed to form a perfect honeycomb structure, with the axes of the hexagonal prisms being aligned with the local maximum heat-extraction

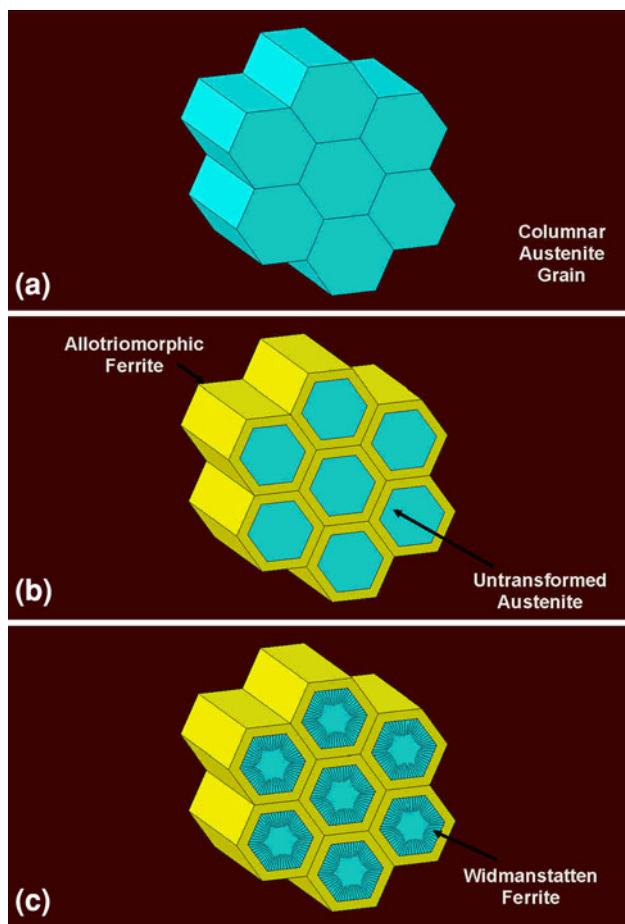


**Fig. 6** Schematic representations of the columnar-grain microstructure in: (a) untransformed austenite, (b) austenite partially transformed into allotriomorphic ferrite, and (c) austenite partially transformed into allotriomorphic and Widmanstätten ferrite

direction. In addition to specifying the shape of the austenite grains, the hexagonal-section edge length,  $a$ , must be specified as, as will be shown below, it affects the final volume fraction of the allotriomorphic ferrite. The hexagonal-section edge length is, in turn, mainly affected by the maximum local cooling rate attained by the liquid during solidification. Specifically,  $a$  decreases with an increase in the maximum local cooling rate of the melt during solidification. To establish functional relationship between the austenite-grain cross-sectional area and the local solidification conditions one must model explicitly melt-solidification aspects of the GMAW process. As this type of modeling is beyond the scope of the present effort, the initial distribution of the austenite grain size within the FZ could not be carried out. Instead, a prototypical value of  $a = 50 \mu\text{m}$  was used throughout the entire FZ [Ref 19]. An effort is underway to couple the present GMAW-process model with the type of GMAW-process model which emphasizes heat transfer from the arc and mass transfer from the electrode to the weld pool, to help establish functional relationships between the GMAW process parameters and the as-cast filler metal material microstructure.

The allotriomorphic ferrite growth model utilized in this study was developed in our recent work [Ref 16] and will be reviewed briefly below. The model is based on the following

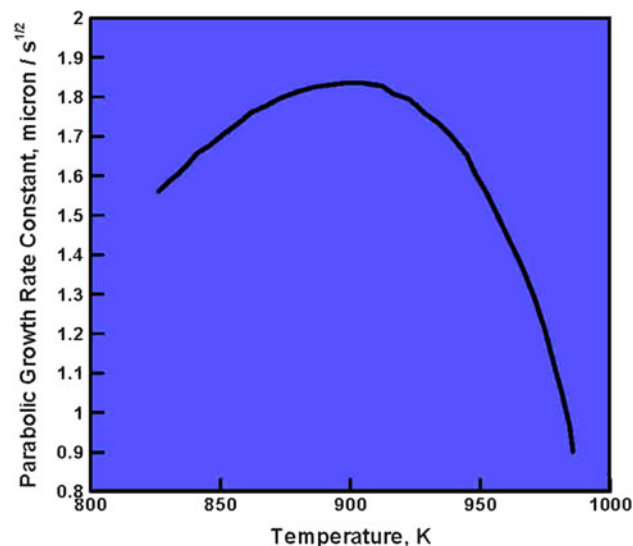


**Fig. 7** Temperature dependence of the one-dimensional parabolic growth rate constant for the austenite → allotriomorphic ferrite phase transformation in MIL A46100 [Ref 19]

postulates: (a) a parabolic relationship exists between the allotriomorphic-ferrite thickness growth rate,  $\frac{dq}{dt}$ , and the instantaneous ferrite-plate thickness,  $q$ , as

$$\frac{dq}{dt} = \frac{\alpha_1(t)}{q}, \quad (\text{Eq 2})$$

where  $\alpha_1(t)$  is a one-dimensional temperature-dependent parabolic-growth-rate constant; (b) the allotriomorphic ferrite finite-plate thickness,  $q_f$ , can be obtained by integrating of Eq 2 between the time at which the growth starts,  $t_i$ , and the time at which the growth ceases,  $t_f$ , along the given temperature history,  $T(t')$ , as

$$q_f = 0.5 \int_{t_i}^{t_f} \alpha_1(T(t')) t'^{-0.5} dt'. \quad (\text{Eq 3})$$

In Eq 3, for any austenite cooling history, time  $t_i$  (and the associated  $\gamma$ -austenite → allotriomorphic ferrite phase transformation-start temperature) are obtained using the aforementioned CCT procedure and the  $F_s$ -labeled, C-shaped curve in Fig. 4 and 5. On the other hand,  $t_f$  (and the associated  $\gamma$ -austenite → allotriomorphic ferrite phase transformation-end temperature) is determined using the same procedure, but by employing  $F_f$  or  $B_s$  C-shaped curves. In other words, transformation of austenite into allotriomorphic ferrite is assumed to cease once kinetically superior austenite → Widmanstätten ferrite or austenite → bainite phase transformations initiate; (c) value of the parabolic-growth rate constant is assumed to be controlled by carbon diffusion within austenite from the advancing allotriomorphic growth front. In other words, following the experimental investigation reported in Ref 3, it is assumed that para-equilibrium conditions exist during the austenite → allotriomorphic ferrite transformation. Using available experimental data [Ref 3, 19], a functional relationship is established between  $\alpha_1$  and temperature in MIL A46100 and this functional relationship is depicted in Fig. 7. Examination of this figure reveals that, as the temperature decreases,  $\alpha_1$  first increases as a result of an increased



thermodynamic driving force for the austenite  $\rightarrow$  allotriomorphic ferrite transformation. On the other hand, at sufficiently low temperatures, the diffusivity of carbon becomes quite low, so that transformation of austenite  $\rightarrow$  allotriomorphic ferrite becomes kinetically controlled, causing a reduction in  $\alpha_1$ ; and (d) finally, it is assumed that a functional relationship can be established between the allotriomorphic ferrite plate thickness,  $q_f$ , and its volume fraction,  $V_{\alpha A}$ . This functional relationship is inferred by applying a simple geometrical computational procedure to the schematic displayed in Fig. 6(b) which depicts a partially transformed section of austenite. The resulting functional relationship can be stated as

$$V_{\alpha A} = \frac{[2q_f \tan(30^\circ)(2a - 2q_f \tan(30^\circ))]}{a^2} \quad (\text{Eq 4})$$

**2.9.3 Widmanstätten-Ferrite Volume Fraction.** Examination of Fig. 5 reveals that, at relatively high transformation temperatures, the onset of austenite to Widmanstätten ferrite phase transformation causes the kinetically sluggish austenite to allotriomorphic ferrite transformation to cease. Following a detailed analysis presented in our recent work [Ref 16], the growth rate of the Widmanstätten ferrite is assumed to be controlled by the rate of lengthening of this lens-shaped phase in a direction normal to the local allotriomorphic ferrite/austenite interface. To help clarify geometrical/topological details related to the formation of Widmanstätten-ferrite, a simple schematic of partially transformed austenite grains is depicted in Fig. 6(c). Examination of this figure reveals the presence of prior austenite grain-boundary regions which have been transformed into allotriomorphic ferrite, as well as lenticular-shaped Widmanstätten plates advancing from the allotriomorphic ferrite/austenite interfaces toward the untransformed austenite grain centers.

As discussed in great detail in our recent work [Ref 16], the rate of the austenite  $\rightarrow$  Widmanstätten-ferrite phase transformation is affected not only by the para-equilibrium condition still present at the ferrite advancing front and the associated carbon diffusion from this front into the untransformed austenite but also by the displacive character of the austenite to Widmanstätten ferrite transformation. Following the procedure described in Ref 6, 20 which is based on the calculation of the Widmanstätten-ferrite area fraction within the austenite grains with hexagonal cross section, Fig. 6(c), the following expression is derived for computing the Widmanstätten-ferrite volume fraction,  $V_{\alpha W}$

$$V_{\alpha W} = C_4 G \left[ \frac{2a - 4q_f \tan(30^\circ) t_{\alpha W}^2}{(2a)^2} \right], \quad (\text{Eq 5})$$

where  $C_4$  ( $=7.367 \text{ s}^{-1}$ , Ref 19) is an alloy-composition-independent constant,  $G$  ( $=52 \text{ } \mu\text{m/s}$ , Ref 19) is the Widmanstätten ferrite lengthening rate, and  $t_{\alpha W}$  is the total time available for the austenite  $\rightarrow$  Widmanstätten ferrite transformation (it should be recalled that once temperature drops below  $B_S$ , the austenite  $\rightarrow$  Widmanstätten ferrite transformation ceases and it is replaced with a austenite  $\rightarrow$  bainite phase transformation).

**2.9.4 Volume Fraction of Bainite.** As mentioned earlier, bainite is a product of austenite-decomposition and the austenite  $\rightarrow$  bainite phase-transformation is of a displacive character but its progress is controlled by carbon diffusion into the untransformed austenite matrix. As established in a series of publications by Bhadeshia and co-workers [Ref 19–21], growth

of bainite involves three distinct processes: (a) nucleation and lengthening of bainite platelets (commonly referred to as subunits) at austenite grain boundaries and phase interfaces. Upon reaching a critical size, lengthening of the bainite subunits is arrested by the plastic deformation accumulated within the surrounding austenite, (b) the transformation then proceeds by nucleation of new subunits ahead of the arrested ones. The newly formed subunits also become arrested and this sequence of processes continues, and (c) the result of the sequential nucleation of bainite subunits is the formation of unit clusters

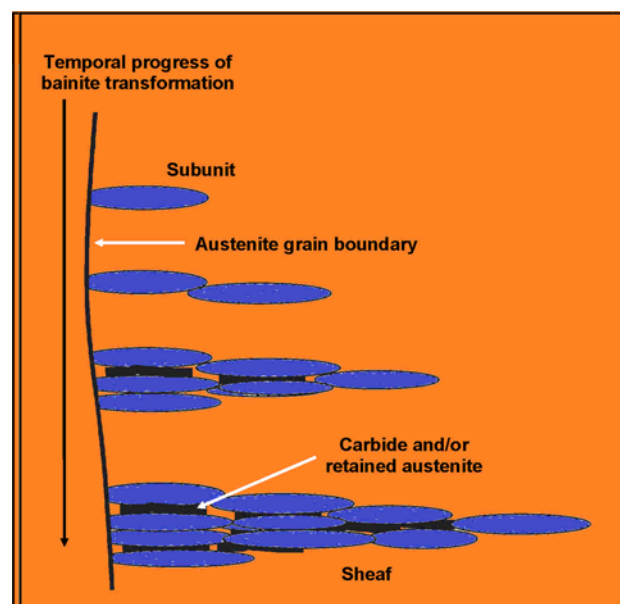


**Fig. 8** Schematic of the bainite growth mechanism via the nucleation of sub-units, their growth and arrest, and subsequent autocatalytic nucleation of new sub-units (resulting in the formation of sub-unit clusters commonly referred to as sheaves) [Ref 21]

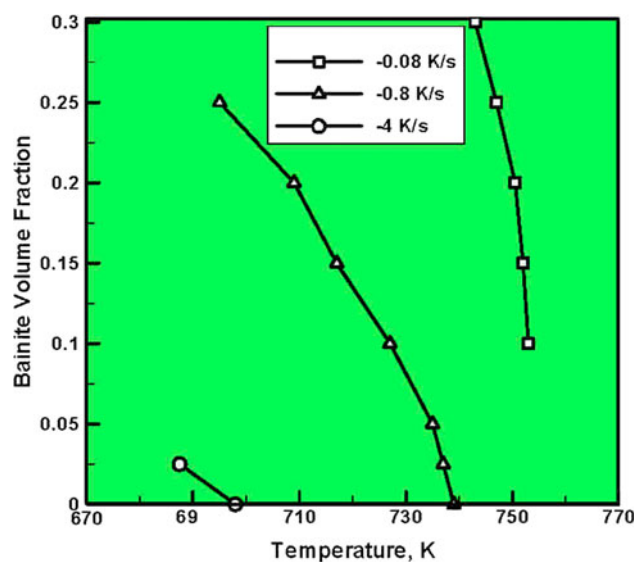


**Fig. 9** The effect of transformation temperature and (constant) cooling rate on the progress of austenite  $\rightarrow$  bainite transformation, in the case of austenite with the TTT and CCT diagrams corresponding to those shown in Fig. 4(a) and 5, respectively

commonly referred to as “sheaves.” It is the rate of lengthening of the sheaves which controls the overall progress of the austenite → bainite phase transformation. A schematic of the bainite-formation mechanism just described is given in Fig. 8.

To determine the rate of the bainitic transformation (and the associated increase in the bainite volume fraction) as a function of time, temperature, chemical composition (and austenite grain size), the model proposed by Matsuda and Bhadeshia [Ref 21] was utilized. This model was fully validated in Ref 21 by comparing its predictions with published isothermal and continuous cooling transformation results. Within this quite elaborate model, the overall rate of increase of the bainite volume fraction is related to the three aforementioned basic processes, and each of these processes is analyzed in great detail. Due to space limitations, details of the model could not be reproduced here. Instead, Fig. 9 shows a set of constant cooling curves which relate the volume fraction of bainite to the instantaneous temperature for the MIL A46100 HAZ section which was described using TTT and CCT diagrams displayed in Fig. 4(a) and 5, respectively. By employing a procedure similar to that described in the case of the allotriomorphic ferrite, the results displayed in Fig. 9 are used in this study to construct a bainite evolution algorithm under arbitrary thermal-history conditions.

**2.9.5 Volume Fraction of Martensite.** As mentioned earlier, when the temperature drops to  $M_S$  all the aforementioned austenite-decomposition phase-transformations are assumed to cease and to be replaced with the kinetically superior diffusionless austenite → martensite phase transformation. This transformation is of an athermal character, i.e., the extent of this transformation depends only on temperature (within the  $M_S$ - $M_f$  range) and not on time. As, as confirmed by the TTT diagrams displayed in Fig. 4(a) to (e),  $M_f$  is above the room temperature, martensitic transformation is expected to cause a complete transformation of austenite. Thus, the volume fraction of martensite,  $V_{Ms}$ , can be computed by simply subtracting the sum of volume fractions of all the room-temperature phases from 1.0.

**2.9.6 Volume Fraction of Other Crystalline Phases.** As established above, complete transformation of austenite to martensite is predicted and, hence, no retained austenite is expected. Other potential phases present at room temperature are not related directly to decomposition of austenite, but rather the results of the precipitation reactions which take place once the solubility limit for austenite is exceeded, during cooling. In MIL A46100, these phases generally include (Ti, V)N and MoC. Room-temperature volume fractions of these phases are approximately predicted by the equilibrium phase diagram, Fig. 3(b).

## 2.10 Phase Volume Fractions within the HAZ

As explained earlier, material points within the HAZ are subjected to more complicated thermal histories which include both heating and cooling portions. The HAZ is operationally defined as a region surrounding the FZ within which these thermal histories cause noticeable and significant changes in the weldment-material microstructure and properties. For convenience, changes in the HAZ material microstructure during heating and cooling portions of the thermal history are analyzed separately.

**2.10.1 Heating Portion of the Thermal History.** As established in section 2, MIL A46100 in its as-received condition typically possesses an auto-tempered martensitic

microstructure. The extent of changes in this microstructure within the HAZ is mainly a function of the maximum-exposure temperature (in the associated “holding” time). Specifically, if the maximum-exposure temperature never exceeds  $A_{c1}$ , the only microstructural changes expected are those associated with tempering of martensite. The outcome of these microstructural changes is the formation of ferrite and, initially,  $\epsilon$ -carbide (or, finally, alloyed cementite). On the other hand, when the maximum-exposure temperature exceeds  $A_{c1}$ , formation of austenite at the prior-austenite grain boundary junctions takes place. A schematic of this martensite to austenite phase

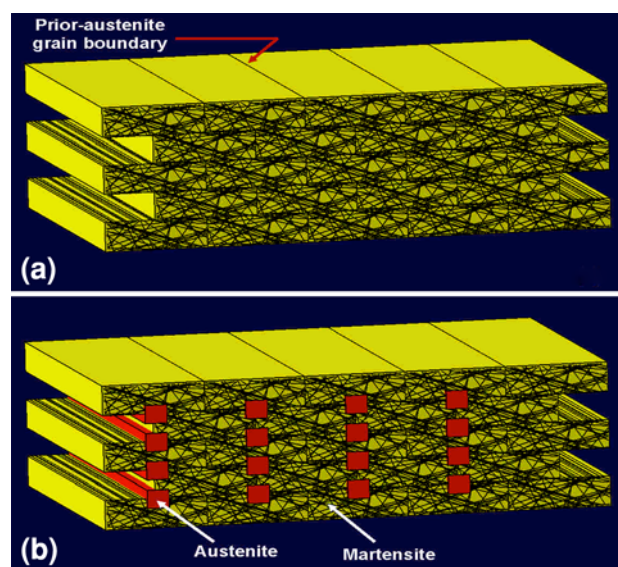


**Fig. 10** A schematic of austenite formation at the prior-austenite grain-boundary junctions within a fully martensitic as-hot-rolled microstructure during super- $A_{c1}$  thermal exposure. (a) Pre-transformation microstructure and (b) post-transformation microstructure

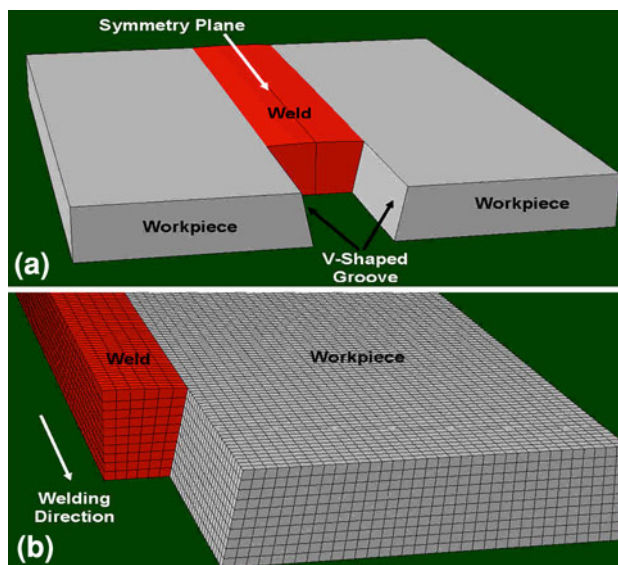


**Fig. 11** Typical (a) geometrical and (b) meshed models used in the present analysis of the GMAW process



transformation is depicted in Fig. 10(a) and (b), in which elongated prior-austenite grains are shown to reveal the effect of hot-rolling on the material microstructure.

In this study, both the carbide-precipitation reactions associated with martensite tempering as well as austenite formation are modeled using an identical approach. That is, in both cases it is assumed that the phase transformations in question, involve nucleation and subsequent growth of the product phases (under para-equilibrium conditions). Following standard practice, the progress of these transformations is represented mathematically using the so-called Kolmogorov-Johnson-Mehl-Avrami (KJMA) relation [Ref 22]. In the case of an isothermal phase transformation, the KJMA relation can be expressed as

$$V_\gamma = V_\gamma^{\text{eq}}(1 - \exp[-\{k(T) \times t\}^n]), \quad (\text{Eq 6})$$

where  $V_\gamma$  and  $V_\gamma^{\text{eq}}$  represent, respectively, the product-phase current and equilibrium volume fractions,  $k(T)$  is a nucleation/growth-rate related kinetic parameter,  $t$  is the isothermal holding time at temperature  $T$ , and  $n$  ( $\approx 1.9$ , Ref 3) is a temperature-invariant exponent. Temperature dependence of  $k$  is normally defined using an Arrhenius-type relation in the form:

$$k(T) = k_0 \times \exp\left(-\frac{Q}{RT}\right), \quad (\text{Eq 7})$$

where  $k_0$  is a pre-exponential constant,  $Q$  is an overall nucleation/growth activation energy for the ferrite to austenite phase transformation, while  $R$  is the universal gas constant. Using multiple-regression analysis and the relevant isothermal kinetics data, the KJMA parameters are determined as follows: (a) for the martensite/austenite transformation,  $k_0 = 1.33 \times 10^5 \text{ s}^{-1}$  [Ref 3],  $Q = 117.07 \text{ kJ/mol}$  [Ref 3]; and (b) for the martensite-tempering reaction,  $k_0 = 4.10 \times 10^5 \text{ s}^{-1}$  [Ref 23, 24],  $Q = 115.50 \text{ kJ/mol}$  [Ref 23, 24].

It is clear that Eq 6 cannot be directly used in the analysis of microstructural changes within the HAZ, as the associated phase transformations proceed under continuous heating (and cooling) conditions, rather than under isothermal holding conditions. Instead, to overcome this problem, a local (continuous) thermal-history function  $T(t)$  can be first approximated, as a sequence of  $N$  isothermal-holding steps each associated with a temperature  $T_i$  ( $i = 1, 2, \dots, N$ ) and of a duration  $\Delta t$ . Then Eq 6 could be used to include the cumulative contributions of all the isothermal-transformation steps as

$$\begin{aligned} V_\gamma(t(T_N)) &= V_\gamma^{\text{eq}} \left( 1 - \exp \left[ - \left\{ \sum_{i=1}^N k(T_i) \times \Delta t \right\}^n \right] \right) \\ &= V_\gamma^{\text{eq}} \left( 1 - \exp \left[ - \left\{ \sum_{i=1}^N k_0 \times \exp \left( -\frac{Q}{RT_i} \right) \times \Delta t \right\}^n \right] \right). \end{aligned} \quad (\text{Eq 8})$$

**2.10.2 Cooling Portion of the Thermal History.** In the case of maximum-exposure temperature being over that  $Ac_1$ , martensite tempering simply continues (at the progressively lower rate) during cooling to room temperature. Thus, the progress of the martensite-tempering phase transformation can be treated using the methods developed in the previous section. As far as the case of a super- $Ac_1$  maximum-exposure temperature is concerned, austenite formed undergoes decomposition during subsequent cooling to room temperature. To a

first order of approximation austenite-decomposition phase transformations can be handled using the same approach as the one developed in the context of FZ. One of the significant differences to be accounted for is the fact that austenite, in the present case if formed within the  $Ac_1$ - $Ac_3$  temperature range possesses a different chemical composition than its counterpart in the FZ. Specifically, due to the hypo-eutectoid character of MIL A46100, austenite formed in this temperature range is enriched on alloying elements relative to the nominal chemical composition of MIL A46100. Consequently, and supported by the results displayed in Fig. 4(a) to (e), austenite is less likely to transform into one of its high-temperature decomposition products, i.e., allotriomorphic ferrite and/or Widmanstätten ferrite. Additional potential difference between the austenite decomposition reactions in HAZ from that in FZ is related to the fact that austenite/ferrite interfaces may already exist at the onset of cooling, hence, ferrite nucleation is not required and the overall progress of austenite to ferrite transformation is controlled by the growth kinetics.

### 3. Computational Procedure

As mentioned earlier, GMAW of MIL A46100 is computationally analyzed in this study using our recently developed transient fully coupled thermo-mechanical finite-element GMAW process model. This model, in turn, was developed by adapting the friction stir welding (FSW) process model developed and applied to a series of armor-grade metallic materials [Ref 25–33]. As details regarding the GMAW process model can be found in Ref 16, only a brief overview of its key elements is given here.

#### 3.1 Geometrical Model

The computational domain comprising two workpieces to be butt-welded possesses a rectangular-parallelepiped shape and has the following dimensions:  $(120 \times 60\text{--}240 \times 15 \text{ mm})$ . The axes of the parallelepiped are aligned with the global  $x$ - $y$ - $z$  Cartesian system, as displayed in Fig. 11(a). The following orientation of the computational domain is chosen: (i) the weld contact interface is set orthogonal to the  $x$ -axis, (ii) the weld gun travels along the  $y$ -axis, while (iii) the workpiece upward normals are aligned with the  $z$ -axis. The origin of the coordinate system is placed at the center ( $x = 0$ )/front ( $y_{\min} = 0$ )/bottom ( $z = 0$ ) point of the computational domain. A V-shaped through-the-thickness groove centered at  $x = 0$  and extending along the  $y$ -axis is created initially by removing the associated workpiece material from the two workpieces to be butt-welded. To mimic groove filling during the GMAW process in the spray metal-transfer mode, the removed material is then progressively added in the  $y$ -direction (to track the motion of the welding gun). In addition, extra material is added during the groove filling process so that the resulting weld acquires a dome shape, Fig. 11(a). It should be noted that the computational domain described above is symmetric about  $x = 0$  and, hence, only one (left, when looking along the direction of motion of the welding gun, in this study) half of this computational domain has to be explicitly analyzed.

#### 3.2 Meshed Model

The selected half of the computational domain is meshed using between 54,000 and 216,000 eight-node, first-order,

thermo-mechanically coupled, reduced-integration, hexahedral continuum elements. Figure 11(b) shows a close-up of the typical meshed model used in this study.

### 3.3 Computational Algorithm

The GMAW computational process model utilized in this study is based on the implementation of a transient, fully coupled, thermo-mechanical, unconditionally stable, implicit finite-element algorithm. At the beginning of the analysis, the computational domain containing the “V-shaped groove” is supported over its bottom ( $z = 0$ ) face, made stress-free and placed at the ambient temperature. As welding proceeds, a high-temperature welding/filler material is progressively added into the groove to track the position of the weld gun. Thermal aspects of the GMAW process are then handled by activating all three basic modes of heat transfer (i.e., conduction, convection, and radiation) between the weld, adjoining workpieces, and the surroundings. The resulting non-uniform thermal fields within the weldment are allowed to produce thermal stresses and, if sufficiently high, give rise to the local permanent deformations/distortions and residual stresses. In the cases when high thermal stresses caused the development of permanent distortions, following the standard practice, 95% of the work of plastic deformation was assumed to be dissipated in the form of heat while the remaining 5% was assumed to be stored in the form of local microstructural and crystal defects.

### 3.4 Initial Conditions

As mentioned above, the workpiece and the welding/filler material are initially assumed to be stress-free but at different temperatures, i.e., (a) the workpiece material is assumed to be at the ambient temperature, while (b) the filler material is assumed to be at the material's solidus temperature (the lowest temperature at which the liquid metal is still present during cooling). It should be noted that in the real GMAW process, the material transferred from the electrode-tip into the groove initially possesses a super-liquidus temperature. No attempt was made in this study to determine this temperature and relate it to the basic welding-process parameters. These shortcomings of the present model will be addressed in our future efforts, which will include coupling of the present GMAW-process model with one of the previously overviewed process models which focus on the aspects of the GMAW process related to the heat and mass transfer from the arc and the electrode, respectively, to the weld pool.

### 3.5 Boundary Conditions

Since only one half of the workpiece/weld assembly is explicitly analyzed, symmetry mechanical and thermal boundary conditions had to be applied across the  $x = 0$  symmetry plane. As far as the additional mechanical boundary conditions are concerned, only the one associated with providing the support to the workpiece over its bottom face is applied. Regarding the additional thermal boundary conditions, natural convection and radiation boundary conditions are prescribed over all exposed surfaces of the workpiece/weld, while the bottom surface is assumed to be insulated.

### 3.6 Mesh Sensitivity

A mesh sensitivity analysis was carried out involving the use of progressively finer finite element meshes to ensure that

the key results and conclusions yielded by this study are not affected by the choice of the computational mesh. The selected finite element mesh(es) represents a compromise between the numerical accuracy and computational efficiency.

### 3.7 Material Model

It should be noted that, in this study, GMAW process modeling and the analysis of the welding-induced microstructural changes are decoupled. In other words, the finite-element-based computational process model described above was used in this study mainly to generate thermal histories of the material points within the FZ and HAZ, while neglecting the contribution of various phase transformations and microstructure-evolution processes (accompanying material cooling within the FZ and the material heating/cooling within the HAZ) to the thermal and mechanical response of the filler-metal and workpiece materials. The resulting thermal histories of the material points within the weld regions are then used within a post-processing analysis (to be presented in section 4) in conjunction with the TTT/CCT austenite-decomposition analyses (presented in section 2) to investigate the role of various phase transformations on the local distribution of the material microstructure and properties within the weld region.

In accordance with the GMAW process model described in the previous paragraph, the filler-metal and workpiece materials are assumed to be homogeneous, single-phase and stable/non-transforming. In addition, the present investigation is carried out under the assumption that the filler-metal is chemically identical to the workpiece material. Consequently, only one material model had to be constructed/utilized. On the other hand, separate sub-models are developed to address mechanical and thermal aspects of the material response. Within the mechanical sub-model, the material's response is assumed to be isotropic (linearly), elastic, and (strain-hardenable, strain-rate sensitive, thermally softenable) plastic. In addition, it is assumed that this response can be mathematically represented using the Johnson-Cook material-model formulation [Ref 34].

Within the Johnson-Cook material-model, the purely elastic response of the material is defined using the generalized Hooke's law, while the elastic/plastic response of the material is described using the following three relations: (a) a *yield criterion*, i.e., a mathematical relation which defines the condition which must be satisfied for the onset (and continuation) of plastic deformation; (b) a *flow rule*, i.e., a mathematical relation which describes the rate of change of different plastic-strain components in the course of plastic deformation; and (c) a *constitutive law*, i.e., a mathematical relation which describes the changes in material strength as a function of the extent of plastic deformation, the rate of deformation, and temperature.

For MIL A46100, as for the most metallic materials, plastic deformation is considered to be of a purely distortional (volume-preserving) character and, consequently, the yield criterion and the flow rule are, respectively, defined using the von Mises yield criterion and a normality flow rule. The von Mises yield criterion states that the (von Mises) equivalent stress (a scalar related to the second invariant of the stress deviator) must be equal to the material yield strength for plastic deformation to occur/proceed. The normality flow-rule, on the other hand, states that the plastic flow takes place in the direction of the stress-gradient of the yield surface (a locus of the stress points within the associated multi-dimensional stress

space at which the von Mises stress criterion is satisfied). The Johnson-Cook strength constitutive law is defined as

$$\sigma_y = A \left[ 1 + \frac{B}{A} (\bar{\epsilon}^{pl})^n \right] \left[ 1 + C \log \left( \dot{\bar{\epsilon}}^{pl} / \dot{\bar{\epsilon}}_0^{pl} \right) \right] \left[ 1 - T_H^m \right], \quad (\text{Eq 9})$$

where  $\bar{\epsilon}^{pl}$  is the equivalent plastic strain,  $\dot{\bar{\epsilon}}^{pl}$  the equivalent plastic strain rate,  $\dot{\bar{\epsilon}}_0^{pl}$  a reference equivalent plastic strain rate,  $A$  the zero-plastic-strain, reference-plastic-strain-rate, room-temperature yield strength,  $B$  the strain-hardening constant,  $n$  the strain-hardening exponent,  $C$  the strain-rate constant,  $m$  the thermal-softening exponent and  $T_H = (T - T_{\text{room}}) / (T_{\text{melt}} - T_{\text{room}})$  a room-temperature ( $T_{\text{room}}$ )-based homologous temperature while  $T_{\text{melt}}$  is the melting (or more precisely, solidus) temperature. All temperatures are given in Kelvin. In Eq 9, the parameter  $A$  defines the as-received material yield strength, the term within the first pair of brackets defines the effect of additional strain hardening, the term within the second pair of brackets quantifies the effect of deformation rate while the last term shows the reversible effect of temperature.

The thermal-portion of the material model is defined using the: (a) material mass density,  $\rho$ , specific heat,  $C_p$ , and thermal conductivity,  $k$ , for the heat-conduction part of the model; (b) the heat transfer coefficient,  $h$ , and the sink temperature,  $T_{\text{sink}} (=T_{\text{room}})$ , for the natural-convection part of the model; and (c) emissivity,  $\epsilon$ , and the ambient temperature,  $T_{\text{amb}} (=T_{\text{room}})$ , for the radiation part of the model. As far as the coupled thermo-mechanical response of the material is concerned, it is quantified using a single parameter, i.e., the coefficient of linear thermal expansion  $\alpha$ .

Tables 1 and 2 provide a summary of the values for all the MIL A46100 mechanical, thermal, and thermo-mechanical model parameters used in this study.

### 3.8 Computational Tool

The GMAW process model based on the aforementioned transient, fully coupled, thermo-mechanical finite element formulation is executed using an implicit solution algorithm implemented in ABAQUS/Standard, a general-purpose finite element solver [Ref 35]. Furthermore, MATLAB, a general-purpose mathematical package [Ref 36], was used to automate ABAQUS input file construction. This was necessary because progressive replacement of the welding/filler material required the use of a large number of computational steps involving mesh models with a continuously increasing number of elements.

## 4. Results and Discussion

The transient fully coupled, thermo-mechanical GMAW model described in the previous section is applied to MIL A46100 to generate a number of results pertaining to the spatial distribution and temporal evolution of a number of thermal, mechanical, and microstructural parameters within the weld region. Due to space limitations, only a few selected results will be presented and discussed in the remainder of this section. Some of these results are presented to merely demonstrate the capabilities of the present approach. For example, the results pertaining to the spatial distribution of the equivalent plastic strain and the residual von Mises stress in the weldment could

be potentially quite important relative to the overall mechanical performance of the GMAW joint. However, these aspects of GMAW modeling are beyond the scope of this study. In sharp contrast, detailed results pertaining to the spatial distribution and temporal evolution of the temperature within the FZ and the HAZ are the key input to the computational analysis (presented in this section) dealing with the prediction of the material microstructure and phase volume fractions, within the weld region.

### 4.1 Selected Results

#### 4.1.1 Temporal Evolution of the Weldment Temperature

**Field.** Figure 12(a) to (d) shows typical results pertaining to the temporal evolution of the temperature field within the weld region. The results displayed in Fig. 12(a), (b), (c), and (d) are obtained at relative welding times of 0, 10, 20, and 30 s, respectively. To improve clarity, regions of the weldment with a temperature lower than 400 K are denoted using light gray. Examination of the results displayed in Fig. 12(a) to (d) reveals that: (a) filling of the groove with the filler-material gives rise to an abrupt increase in temperature in the region next to the workpiece/weld interface; (b) as welding proceeds, natural convection and radiation to the surroundings, together with conduction through the adjacent material region, cause the previously deposited filler material to cool; and (c) by monitoring the expansion of the 400 K temperature contour over the workpiece top surface, one can visualize the propagation of the thermal-conduction wave within the workpiece.

#### 4.1.2 Temporal Evolution of Temperature Within the FZ and HAZ.

Temporal evolution of temperature within the FZ and HAZ is exemplified using the results displayed in Fig. 13(a) and (b). The results displayed in Fig. 13(a) pertain to

**Table 1 Johnson-Cook strength model material parameters for MIL A46100**

| Parameter                  | Symbol            | Units | Value       |
|----------------------------|-------------------|-------|-------------|
| Young's modulus            | $E$               | GPa   | 205-215     |
| Poisson's ratio            | $\nu$             | N/A   | 0.285-0.295 |
| Reference strength         | $A$               | MPa   | 1000-1100   |
| Strain-hardening parameter | $B$               | MPa   | 250.0       |
| Strain-hardening exponent  | $n$               | N/A   | 0.12        |
| Strain-rate coefficient    | $C$               | N/A   | 0.02        |
| Room temperature           | $T_{\text{room}}$ | K     | 298.0       |
| Melting temperature        | $T_{\text{melt}}$ | K     | 1720        |
| Temperature exponent       | $m$               | N/A   | 0.5         |

**Table 2 General, Thermo-mechanical, and thermal parameters for MIL A46100**

| Parameter                               | Symbol            | Units                | Value   |
|---|-------------------|----------------------|---------|
| Material mass density                   | $\rho$            | kg/m <sup>3</sup>    | 7850    |
| Coefficient of linear thermal expansion | $\alpha$          | 1/K                  | 11.5e-6 |
| Specific heat                           | $C_p$             | J/kg · K             | 480     |
| Thermal conductivity                    | $k$               | W/m · K              | 42      |
| Heat transfer coefficient               | $h$               | W/m <sup>2</sup> · K | 45      |
| Sink temperature                        | $T_{\text{sink}}$ | K                    | 298     |
| Emissivity                              | $\epsilon$        | N/A                  | 0.77    |
| Ambient temperature                     | $T_{\text{amb}}$  | K                    | 298     |



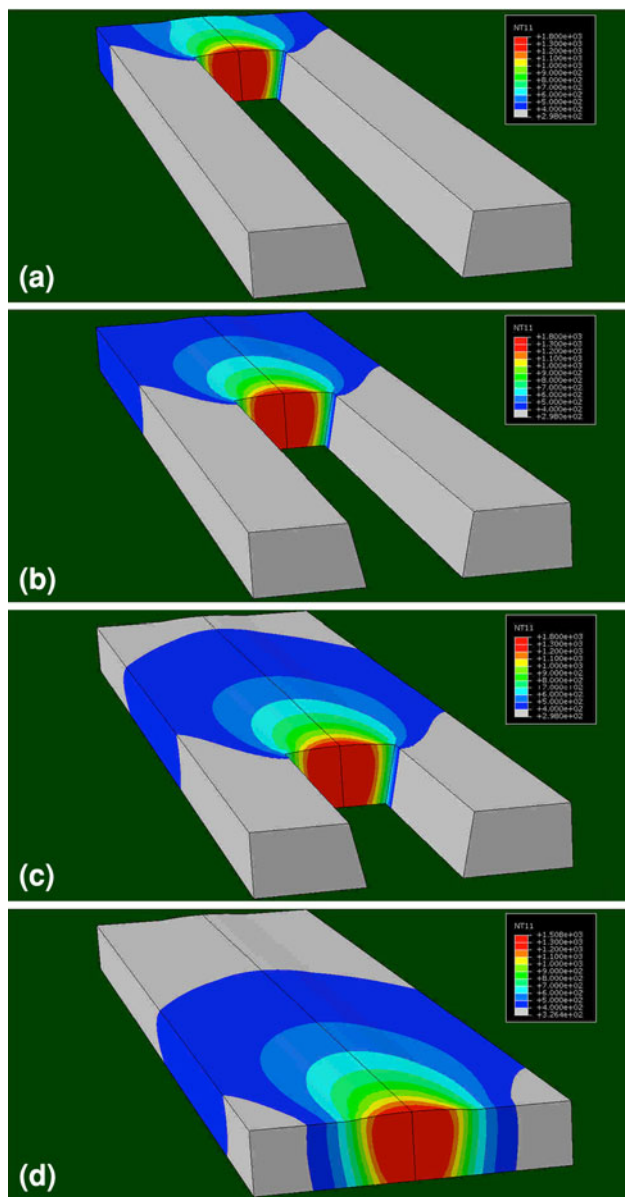


**Fig. 12** An example of typical results pertaining to the spatial distribution and temporal evolution of temperature in the weld region at relative welding times of: (a) 10 s, (b) 20 s, (c) 30 s, and (d) 40 s

the weldment mid-plane within the FZ and the curve labels used represent the distance of the material point in question from the weld  $y$ - $z$  symmetry plane. The results displayed in Fig. 13(b), on the other hand, pertain to the weldment mid-plane within the HAZ where the curve labels used, in this case, represent the distance of the material point in question from the FZ/HAZ interface. It should be noted that the results, such as those displayed in Fig. 13(a) and (b), but for a substantially larger number of closely spaced material points, are used in the next section to determine the phase volume fractions in the FZ and HAZ. Examination of the results displayed in Fig. 13(a) and (b) reveals that: (a) material residing within the FZ, which initially had a temperature equal to the solidus temperature of MIL A46100, undergoes continuous cooling during the GMAW simulation process; (b) as expected, material points within the FZ which are closest to the FZ/HAZ interface experience the highest cooling rate (as the workpieces are initially at the room

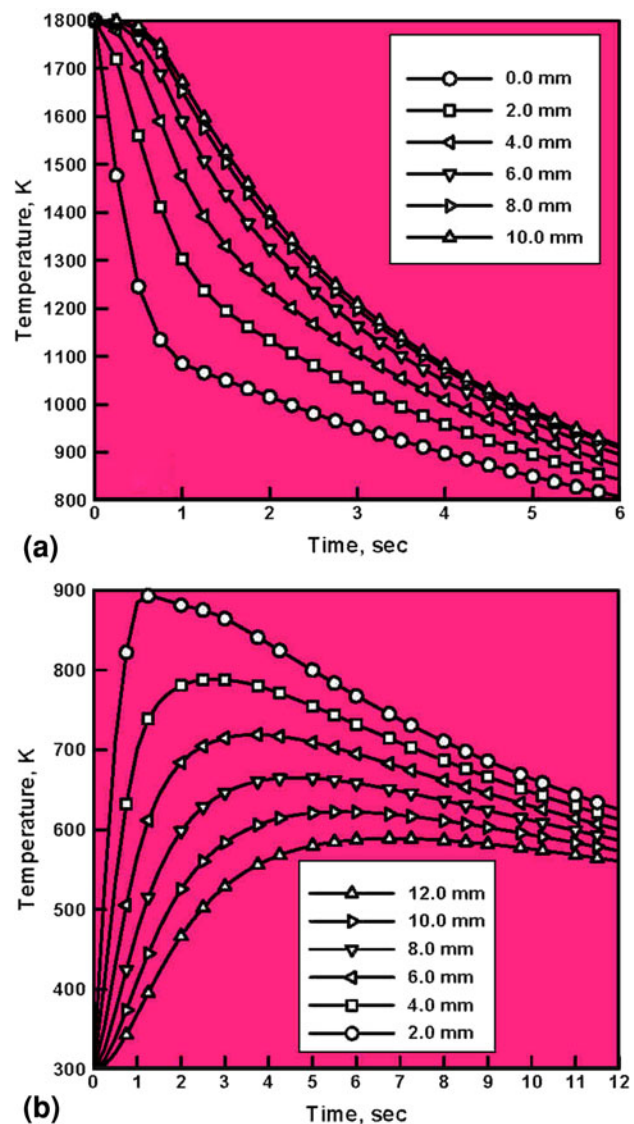


**Fig. 13** An example of typical results pertaining to the temporal evolution of temperature: (a) along the workpiece mid-plane within the FZ (the labels used represent the distance of the material point in question from the weld  $y$ - $z$  symmetry plane) and (b) along the workpiece mid-plane within the HAZ (the labels used represent the distance of the material point in question from the HAZ/FZ interface)

temperature and act as chillers); (c) in comparison, material points within the HAZ experience a significantly more complex heating/cooling thermal history; and (d) material points within the HAZ which are closest to the workpiece/weld interface experience the maximum temperature during the GMAW process, due to the presence of initially very hot filler material within the FZ.

**4.1.3 Thermal Strains and Residual Stresses.** Large thermal gradients in the weld regions surrounding the FZ/HAZ interfaces produce thermal stresses which, if sufficiently high, can give rise to plastic deformations. In such cases, weldments will develop residual stresses during cooling to room temperature. As explained earlier, due to its thermo-mechanical character, the present GMAW model can predict the development of such plastic strains and residual stresses. Examples of the thermal strain/residual stress results obtained using the present GMAW model are shown in Fig. 14(a) and (b).

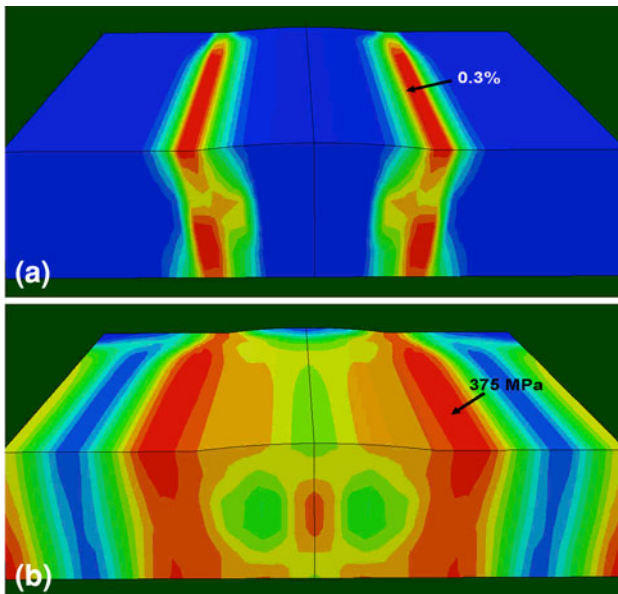


**Fig. 14** An example of typical results pertaining to the spatial distribution of: (a) equivalent plastic strain and (b) residual von Mises equivalent stress over a transverse section of the weld and the work-piece region adjacent to the weld

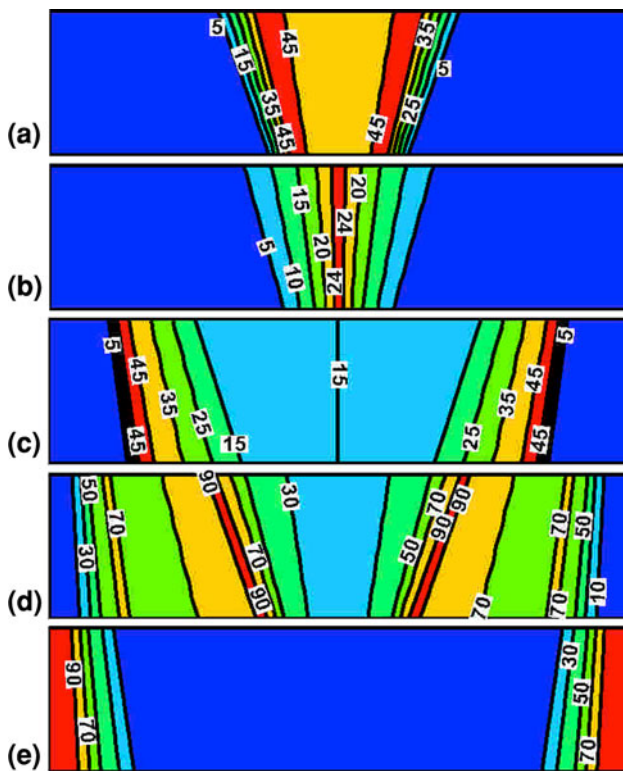


**Fig. 15** An example of typical results pertaining to the spatial distribution of phase volume fraction for: (a) allotriomorphic ferrite, (b) Widmanstätten ferrite, (c) bainite, (d) fresh martensite, and (e) tempered martensite over a transverse section of the weld and the work-piece region adjacent to the weld

Figure 14(a) and (b) shows, respectively, spatial distribution of the equivalent plastic strain and the von Mises stress over a transverse section of the weld. For improved clarity, contour-level

legends are not displayed, but instead, the maximum values of the equivalent plastic strain and the von Mises residual stress are denoted in these figures. Examination of the results displayed in Fig. 14(a) and (b) shows that, as anticipated, the largest plasticity/residual stress effects are observed in the regions surrounding the HAZ/FZ interfaces. It should be noted that the austenite  $\rightarrow$  bainite and austenite  $\rightarrow$  martensite phase transformations, due to their displacive character, are expected to be affected by the observed plastic strains and residual stresses through the so-called deformation-induced and stress-assisted transformation effects [Ref 37–39]. However, inclusion of these phenomena is beyond the scope of this study, but will be addressed in our future efforts.

## 4.2 Room-Temperature Weld Microstructure Prediction

In this section, the thermal history results like the ones reported in Fig. 13(a) and (b) are used as input to the FZ and HAZ microstructure-evolution analyses presented in section 2 to determine the room-temperature volume fractions of all the crystalline phases within the weld region. It should be recalled that the microstructure evolution analyses presented in section 2 revealed that the nature of the phase transformations encountered and their thermodynamic/kinetic relations are drastically different for the materials residing within the FZ and the HAZ. As a result, different microstructural-evolution functional relationships were applied, in this portion of the work, to the material points residing in these two portions of the weld region. The results pertaining to the spatial variation of the phase volume fractions within the FZ and the HAZ are ultimately combined to construct the corresponding contour plots for the entire weld region. It should be noted that all the analyses carried out in this portion of the work pertain to the case of MIL A46100, initially in the as-hot-rolled and self-tempered martensitic state. Based on this assumption, and considering details of the microstructure-evolution analyses presented in section 2, any portion of the weld region may contain up to five crystalline-phases/microconstituents: (a) allotriomorphic ferrite, (b) Widmanstätten ferrite, (c) bainite, (d) freshly formed martensite, and (e) tempered martensite.

An example of the results obtained using the aforementioned procedure is depicted in Fig. 15(a) to (e). These figures display the spatial distribution of phase volume fractions for: (a) allotriomorphic ferrite, (b) Widmanstätten ferrite, (c) bainite, (d) freshly formed martensite, and (e) tempered martensite over a transverse section of the weld and the workpiece region adjacent to the weld. Examination of the results displayed in Fig. 15(a) to (e) reveals that:

- Allotriomorphic and acicular ferrites are present only within the FZ, as seen in Fig. 15(a) and (b), and this finding is fully consistent with the fact that the material within this region was initially at the solidus temperature (the highest temperature found within the weld region), undergoes relatively slow cooling and possesses relatively low hardenability (as austenite chemical composition is nearly identical to that of the alloy itself);
- Due to the lower cooling rates and the low hardenability of austenite within the FZ, the volume fraction of freshly formed martensite is relatively low in this region,  $<30\%$ , Fig. 15(d). However, the volume fraction of this phase abruptly increases to ca. 90% at the FZ/HAZ interface and remains at this level within a short distance



from the FZ/HAZ interface. These findings are mainly the result of lower cooling rates in this region, as the material is fully austenitized (i.e., the maximum exposure temperature exceeds  $A_{c3}$ ) in this HAZ region and is effectively of the same chemical composition as the alloy itself;

- (c) As the distance from the FZ/HAZ interface increases, the volume fraction of freshly formed martensite first decreases. This finding is consistent with the fact that, within this fully austenitized HAZ region, the cooling rate decreases with an increase in the distance from the FZ/HAZ interface. As the distance from the FZ/HAZ interface is further increased, the maximum exposure temperature falls below  $A_{c3}$  and only partial austenitization takes place. However, the austenite formed possesses a higher hardenability as it is richer in alloying elements than the alloy itself. Consequently, as distance from the FZ/HAZ interface increases (in this HAZ region), the volume fraction of martensite first decreases and then increases. Ultimately, the volume fraction of martensite drops to zero at the locus of HAZ points at which the maximum exposure temperature becomes  $A_{c1}$ . At still further distances from the FZ/HAZ interface, austenitization of the initial microstructure does not take place and, hence, the volume fraction of freshly formed martensite remains zero;
- (d) Since the austenite  $\rightarrow$  bainite phase transformation is mainly competing with the austenite  $\rightarrow$  martensite phase transformation, variation of the volume fraction of bainite throughout the FZ and within the HAZ (as a function of distance from the FZ/HAZ interface), Fig. 15(c) can be understood as a consequence of this competition; and
- (e) Tempered martensite is not present in the FZ, or within the portion of the HAZ which was fully austenitized, as shown in Fig. 15(e). In the remainder of the HAZ, volume fraction of tempered martensite increases with distance from the FZ/HAZ interface and reaches the value of ca. 100%, at a locus of the HAZ points with a maximum exposure temperature of  $A_{c1}$ .

#### 4.3 Model Validation

The analysis of the results pertaining to the spatial distribution of various crystalline phases and microstructural constituents within the MIL A46100 weld region, presented in the previous section, confirmed that the predictions made by the present GMAW process model are in good qualitative agreement with general expectations/observations. Unfortunately, quantitative validation of the present model cannot be carried out for a number of reasons: (a) as explained earlier, the present GMAW process model does not allow direct correlation between the GMAW process parameters and the spatial distribution of material microstructure within the FZ and HAZ. For example, within the present model, initial temperature of the weld-pool is set equal to the material solidus temperature and no provision is available for relating this temperature to the GMAW process parameters. As mentioned earlier, this shortcoming of the current model will be rectified in our future work; (b) GMAW experimental facilities are currently being developed/assembled to support the ongoing GMAW modeling and simulation efforts. Once these facilities have been completed, they will enable a full quantitative validation of the present GMAW model; and (c) no open-literature experimental results pertaining to

the spatial distribution of various crystalline phases and microstructures within the weld region, for the case of MIL A46100 workpiece material and MIL A46100 filler material could be found. In Ref 15 weld microstructure results are presented for the case of MIL A46100 workpiece material and AWS E11018M filler material. Chemical analysis results obtained in Ref 15 revealed that significant solid state diffusion takes place within the HAZ near the FZ/HAZ interface. These diffusion effects alter locally the material chemistry and, hence, relative stability of different crystalline phases (as quantified by the corresponding phase, TTT and CCT diagrams). Consequently, the microstructure distribution results within the FZ and the HAZ portion affected by solid state diffusion reported in Ref. 15 could not be directly compared with the present computational results. However, such a comparison had been made for the HAZ region, which is further away from the FZ/HAZ interface. This comparison revealed that the two sets of results are mutually consistent. As mentioned earlier fully quantitative comparison will be possible only after the present GMAW process model is upgraded to include the effects of process parameters.

## 5. Summary and Conclusions

Based on the study presented and discussed in this manuscript, the following main summary remarks and conclusions can be made:

1. A fully coupled thermo-mechanical finite element model has been developed for the conventional GMAW process. Two-way thermo-mechanical coupling is achieved by (i) accounting for temperature dependence of the main material properties of the workpiece and filler-metal and (ii) accounting for dissipation of the work of plastic deformation (which may result from the presence of high thermal and/or residual stresses).
2. The GMAW process model developed is capable of predicting spatial distribution and temporal evolution of various thermo-mechanical quantities such as temperature, plastic strains, residual stresses, etc. These process-model outputs are critical inputs to a computational analysis aimed at predicting spatial distribution of the as-welded material microstructure, including volume fractions of various crystalline phases. Such a computational analysis is developed in this study for the material of interest, i.e., armor-grade martensitic steel MIL A46100.
3. Application of the GMAW process model and the microstructure-evolution computational analysis yielded the results pertaining to the spatial distribution of the volume fractions of various crystalline phases and microconstituents within the MIL A46100 GMAW FZ and HAZ. These findings are found to be in good qualitative agreement with general experimental observations/findings reported in the open literature.
4. Issues related to further advancements in the model as well as a more quantitative validation of the present model are also discussed.

## Acknowledgments

The material presented in this article is based on the study supported by two Army Research Office sponsored grants

(W911NF-11-1-0207 and W911NF-09-1-0513) and two US Army/Clemson University Cooperative Agreements (W911NF-04-2-0024 and W911NF-06-2-0042). The authors are indebted to Dr. Larry C. Russell, Jr. of ARO for his continuing support and interest in this study.

## References

1. M.G.H. Wells, R.K. Weiss, and J.S. Montgomery, "LAV armor plate study", *MTL TR 92-26*, US Army Materials Technology Laboratory, Watertown, MA, 1992
2. A.D. Althouse, C.H. Turnquist, W.A. Bowditch, K.E. Bowditch, and M.A. Bowditch, Gas Metal Arc Welding, *Modern Welding*, 10th ed., Goodheart-Willcox Publisher, Tinley Park, IL, 2004, p 233–265
3. W. Zhang, J.W. Elmer, and T. DebRoy, Modeling and Real Time Mapping of Phases During GTA Welding of 1005 Steel, *Mater. Sci. Eng., A*, 2002, **333**, p 320–335
4. Ø. Grong, *Metallurgical Modelling of Welding*, 2nd ed., The Institute of Materials, London, 1997
5. K. Easterling, *Introduction to the Physical Metallurgy of Welding*, 2nd ed., Butterworth Heinemann, Boston, 1992
6. L.-E. Svensson, *Control of Microstructures and Properties in Steel Arc Welds*, CRC Press, Boca Raton, 1994
7. R. Mancini and C. Budde, Reaustenitisation in Fe-C Steels Revisited, *Acta Mater.*, 1999, **47**, p 2907–2911
8. R.C. Reed, T. Akbay, Z. Shen, J.M. Robinson, and J.H. Root, Determination of Reaustenitisation Kinetics in a Fe-0.4C Steel Using Dilatometry and Neutron Diffraction, *Mater. Sci. Eng., A*, 1998, **256**, p 152–165
9. J.H. Valentich, *Tube Type Dilatometers: Applications From Cryogenic to Elevated Temperatures*, Instrument Society of America, Research Triangle Park, NC, 1981
10. J. Haidar, A Theoretical Model for Gas Metal Arc Welding and Gas Tungsten Arc Welding. I, *J. Appl. Phys.*, 1998, **84**, p 3518–3529
11. J. Haidar, Prediction of Metal Droplet Formation in Gas Metal Arc Welding. II, *J. Appl. Phys.*, 1998, **84**, p 3530–3540
12. J. Haidar, An Analysis of Heat Transfer and Fume Production in Gas Metal Arc Welding. III, *J. Appl. Phys.*, 1998, **85**, p 3448–3459
13. J. Hu and H.L. Tsai, Heat and Mass Transfer in Gas Metal Arc Welding. Part I: The Arc, *Int. J. Heat Mass Transf.*, 2007, **50**, p 833–846
14. J. Hu and H.L. Tsai, Heat and Mass Transfer in Gas Metal Arc Welding. Part II: The Metal, *Int. J. Heat Mass Transf.*, 2007, **50**, p 808–820
15. S.J. Unfried, C.M. Garzón, and J.E. Giraldo, Numerical and Experimental Analysis of Microstructure Evolution During Arc Welding in Armor Plate Steels, *J. Mater. Process. Technol.*, 2009, **209**, p 1688–1700
16. M. Grujicic, S. Ramaswami, J.S. Snipes, R. Yavari, A. Arakere, C.-F. Yen and B.A. Cheeseman, Computational Modeling of Microstructure Evolution in AISI 1005 Steel During Gas Metal Arc Butt Welding, *J. Mater. Eng. Perform.*, 2012. doi:10.1007/s11665-012-0402-1
17. MIL STD-A46100 Standard specification, 1983: Armor plate steel wrought high hardness
18. J.-O. Andersson, T. Helander, L. Höglund, P. Shi, and B. Sundman, Calphad-Based Thermocalc and Dictra Method, *Calphad*, 2002, **26**, p 273–312
19. H.K.D.H. Bhadeshia, L.-E. Svensson, and B. Grestoft, A Model for the Development of Microstructure in Low-Alloy Steel (Fe-Mn-Si-C) Weld Deposits, *Acta Metall.*, 1985, **33**, p 1271–1283
20. S.J. Jones and H.K.D.H. Bhadeshia, Kinetics of the Simultaneous Decomposition of Austenite into Several Transformation Products, *Acta Mater.*, 1997, **45**, p 2911–2920
21. H. Matsuda and H.K.D.H. Bhadeshia, Kinetics of the Bainite Transformation, *Proc. R. Soc. Lond. A*, 2004, **460**, p 1707–1722
22. P. Kruger, On the Relation Between Non-isothermal and Isothermal Kolmogorov-Johnson-Mehl-Avrami Crystallization Kinetics, *J. Phys. Chem. Solids*, 1993, **54**, p 1549–1555
23. M. Grujicic and G. Haidemenopoulos, Treatment of Paraequilibrium, Thermodynamics in an AF1410 Steel Using the Thermo-calc Software and, Database, *Calphad*, 1988, **12**, p 219–224
24. M. Grujicic, Thermodynamics Aided Design of High Co-Ni Secondary Hardening Steels, *Calphad*, 1990, **14**, p 49–59
25. M. Grujicic, B. Pandurangan, C.-F. Yen, and B.A. Cheeseman, Modifications in the AA5083 Johnson-Cook Material Model for Use in Friction Stir Welding Computational Analyses, *J. Mater. Eng. Perform.*, 2011. doi:10.1007/s11665-011-0118-7
26. M. Grujicic, G. Arakere, B. Pandurangan, J. M. Ochterbeck, C.-F. Yen, B. A. Cheeseman, A. P. Reynolds, and M. A. Sutton, Computational Analysis of Material Flow During Friction Stir Welding of AA5059 Aluminum Alloys, *J. Mater. Eng. Perform.*, 2011. doi:10.1007/s11665-011-0069-z
27. M. Grujicic, G. Arakere, A. Hariharan, B. Pandurangan, C.-F. Yen, and B.A. Cheeseman, Two-level Weld-Material Homogenization Approach for Efficient Computational Analysis of Welded Structure Blast Survivability, *J. Mater. Eng. Perform.*, 2010. doi:10.1007/s11665-011-9876-5
28. M. Grujicic, G. Arakere, A. Hariharan, and B. Pandurangan, A Concurrent Product-development Approach for Friction-Stir Welded Vehicle-Underbody Structures, *J. Mater. Eng. Perform.*, 2012, **21**, p 437–449
29. M. Grujicic, G. Arakere, B. Pandurangan, A. Hariharan, C.-F. Yen, B.A. Cheeseman, and C. Fountzoulas, Computational Analysis and Experimental Validation of the Ti-6Al-4V Friction Stir Welding Behavior, *J. Eng. Manuf.*, 2010, **224**, p 1–16
30. M. Grujicic, G. Arakere, B. Pandurangan, A. Hariharan, C.-F. Yen, and B.A. Cheeseman, Development of a Robust and Cost-effective Friction Stir Welding Process for use in Advanced Military Vehicle Structures, *J. Mater. Eng. Perform.*, 2011, **20**, p 11–23
31. M. Grujicic, G. Arakere, C.-F. Yen, and B.A. Cheeseman, Computational Investigation of Hardness Evolution During Friction-Stir Welding of AA5083 and AA2139 Aluminum Alloys, *J. Mater. Eng. Perform.*, 2011, **20**, p 1097–1108
32. M. Grujicic, G. Arakere, H.V. Yalavarthy, T. He, C.-F. Yen, and B.A. Cheeseman, Modeling of AA5083 Material-Microstructure Evolution During Butt Friction-Stir Welding, *J. Mater. Eng. Perform.*, 2010, **19**, p 672–684
33. M. Grujicic, T. He, G. Arakere, H.V. Yalavarthy, C.-F. Yen, and B.A. Cheeseman, Fully-Coupled Thermo-mechanical Finite-Element Investigation of Material Evolution During Friction-Stir Welding of AA5083, *J. Eng. Manuf.*, 2010, **224**, p 609–625
34. G.R. Johnson and W.H. Cook, A Constitutive Model and Data for Metals Subjected to Large Strains, High Strain Rates and High Temperatures, *Proceedings of the 7th International Symposium on Ballistics*, 1983
35. ABAQUS Version 6.10EF, *User Documentation*, Dassault Systems, 2011
36. MATLAB, *The Language of Technical Computing*, Version 8.0.0.783, R2012b. The MathWorks Inc., MA
37. M. Gore, M. Grujicic, G.B. Olson, and M. Cohen, Thermally Activated Grain Boundary Unpinning, *Acta Metall.*, 1989, **37**, p 2849–2854
38. M. Grujicic and G.B. Olson, Dynamics of Martensitic Interfaces, *Interface Sci.*, 1998, **6**, p 155–164
39. M. Grujicic and N. Sankaran, Dispersed-Phase Martensitic Transformation Controlled Deformation Behavior of Two-Phase Metallic Materials, *Int. J. Solids Struct.*, 1997, **34**, p 4421–4446